arXiv:2104.14881v2 [hep-ph] 10 Aug 2021

Consistent explanation for the cosmic-ray positron excess in p-wave Sommerfeld-enhanced dark matter annihilation

Yu-Chen Ding[a], Yu-Lin Ku[a], Chun-Cheng Wei[a], and Yu-Feng Zhou[a,b]

[a] *CAS key laboratory of theoretical Physics, Institute of Theoretical Physics, Chinese Academy of Sciences, Beijing 100190, China; School of Physics, University of Chinese Academy of Sciences, Beijing 100049, China;* [b] *School of Fundamental Physics and Mathematical Sciences, Hangzhou Institute for Advanced Study, UCAS, Hangzhou 310024, China; International Centre for Theoretical Physics Asia-Pacific, Beijing/Hangzhou, China.*

(Dated: February 27, 2022)

Abstract

Sommerfeld-enhanced dark matter (DM) annihilation through s-wave has been widely considered as a consistent explanation for both the observed cosmic-ray (CR) positron excess and the DM thermal relic density. However, as the s-wave Sommerfeld-enhanced annihilation cross section increases monotonically with decreasing DM velocity, severe constraints appear from the data of gamma rays from dwarf spheroidal satellite galaxies (dSphs) and the cosmic microwave background (CMB), as the relevant typical DM velocities are even lower than that in the Galactic halo. In this work, we consider Sommerfeld-enhanced p-wave DM annihilation where the DM annihilation cross section can be enhanced at certain velocities but eventually be highly suppressed when the DM velocities become extremely low. We calculate the velocity-dependent astrophysics factors (J-factors) for the Sommerfeld-enhanced p-wave DM annihilation for fifteen nearby dSphs. Taking the channel of DM annihilating into 4μ through two light mediators as an example, we show that there are parameter regions where this mechanism can account for the CR positron excess and the DM relic density, while being compatible with the constraints from dSphs gamma rays measured by Fermi-LAT and that from the CMB measured by PLANCK.

I. INTRODUCTION

Numerous astrophysical observations indicate that non-baryonic cold dark matter (DM) constitutes $\sim 84\%$ of the total matter of the Universe [1]. However, the particle nature of DM remains largely unknown. Weakly-interacting massive particles (WIMPs) are one of the popular DM candidates which can naturally obtain the observed DM abundance through self-annihilation into the standard model (SM) final states during the process of thermal freeze-out. If DM particles in the Galactic halo can annihilate into SM stable final states, they can make extra contributions to the fluxes of cosmic-ray (CR) particles which can be probed by the current DM indirect detection experiments.

CR antiparticles, such as CR positrons and antiprotons, are considered to be relatively rare as they are CR secondaries produced dominantly from the collisions between primary CRs and the interstellar gas. Thus they are expected to be sensitive to extra contributions, and are important probes of DM interactions. In recent years, a number of experiments such as PAMELA [2], Fermi-LAT [3] and AMS-02 [4] have reported an excess of CR positron flux starting at positron energy above ~ 10 GeV and peaking at ~ 300 GeV, which strongly suggests the existence of nearby extra positron sources. The excess may have astrophysical origins, such as nearby pulsar wind nebulae (see e.g. [5–8]), and supernovae remnants (e.g. [9–11]), etc.. DM annihilation or decay in the Galactic halo can also be a possible explanation [12–17]. In the scenario of DM annihilation, the favored DM typical particle mass is $m_\chi \sim \mathcal{O}(0.5-1)$ TeV and velocity-weighted annihilation cross section $\langle\sigma_{\rm ann}v_{\rm rel}\rangle \sim \mathcal{O}(10^{-24})$ cm^3 s^{-1}, which depends on annihilation channels [13, 14, 18, 19]. The favored DM parameter space is, however, strongly constrained by other observations. For instance, DM annihilation directly into quark and gauge boson pairs ($\bar{q}q$, W^+W^- and Z^0Z^0) is ruled out by the lack of corresponding excesses in the CR antiproton flux [20]. For leptonic channels, DM particles dominantly annihilating into $2\tau/4\tau$ leads to a good fit to the AMS-02 data. However, this channel produces significant amount of gamma rays, which is ruled out by Fermi-LAT observations on gamma rays from dwarf spheroidal satellites galaxies (dSphs) [21]. The $\mu^+\mu^-$ (2μ) and $\mu^+\mu^-\mu^+\mu^-$ (4μ) channels produce much less gamma rays and thus only have mild tensions with the Fermi-LAT gamma-ray data. Compared with the 2μ channel, the 4μ channel predicts a broader positron excess, which is in a better agreement with the AMS-02 data.

If the DM annihilation cross section remains constant (velocity independent) during different epochs of the Universe, there exist other severe constraints. For instance, for WIMP DM candidates, very strong constraint arises from the DM relic density. The same DM annihilation cross section at the epoch of thermal freeze-out should be responsible for its relic density, which sets a typical scale of $\langle\sigma_{\rm ann}v_{\rm rel}\rangle \sim 3\times10^{-26}$ cm$^3\cdot$s^{-1}, which is about two orders of magnitude lower than that required to explain the observed CR positron excess, which is often referred to as the "boost factor" problem for DM explanation [13, 18]. It is very unlikely that the local DM density clumps can provide such a large boost factor [22, 23].

During the epoch of recombination, the charged particles produced by DM annihilation can modify the cosmic microwave background (CMB) [24–28]. The precise measurements of CMB temperature and polarization anisotropy performed by Planck have set upper limits on DM annihilation cross section [1]. For some DM annihilation channels, the constraints from CMB are more stringent than that derived from dSphs gamma-ray observations.

Since the typical velocity of DM particles varies significantly in different epochs and regions of the Universe, a possible solution to reconcile these apparent tensions is to introduce velocity- or temperature-dependent DM annihilation cross sections. An extensively studied mechanism is the Sommerfeld enhancement [29–37]. The Sommerfeld enhancement of annihilation cross section occurs when the annihilating particles self-interact through a long-range attractive potential at low velocities. In this scenario, the short-distance DM annihilation cross-section can be greatly enhanced due to the distortion of the wave functions of annihilating particles at origin. The attractive potential may originate from multiple-exchange of light force-carrier particles between the annihilating DM particles. The s-wave Sommerfeld enhancement has been considered to reconcile the apparent tension between CR positron excess and the thermal relic density in WIMP scenarios, as the DM typical relative velocities $v_{\rm rel}$ in the Galactic halo and at the freeze-out are $\sim 10^{-3}c$ and $\sim 10^{-1}c$, respectively [30, 32, 33, 38–40], where c is the speed of light. For simple models with a vector mediator, the allowed parameter space is quite limited, as the DM annihilation cross section also receives contributions from DM annihilating into light mediators [41]. But for more complicated models, such as the exciting DM model there still exists large parameter space to explain the data [42]. Note, however, that the s-wave Sommerfeld-enhanced annihilation cross section increases monotonically with decreasing DM velocity, which makes it even more difficult to reconcile other constraints such as that from the data of dSphs gamma rays and CMB, as the related typical velocity is even lower $\sim 10^{-4}c$ and $\sim 10^{-8}c$, respectively [39, 43–53].

In this work, we consider DM particles annihilating through p-wave with Sommerfeld enhancement. The p-wave Sommerfeld-enhanced cross section no longer increases monotonically towards lower DM velocity, since the cross section before the enhancement has significant velocity dependence $\sigma_{\rm ann}v_{\rm rel} \sim v_{\rm rel}^2$. After including the effect of Sommerfeld enhancement, the DM total annihilation cross section can be enhanced at some velocities, but eventually be suppressed towards the limit $v \to 0$. Thus it opens the possibility of reconciling the above mentioned tensions. In this work, we consider a typical DM annihilation channel of $\chi\chi \to 2\phi \to 4\mu$, where ϕ is the mediator particle and also the force-carrier. We calculate the velocity-dependent astrophysics factors (J-factors) for the Sommerfeld-enhanced p-wave DM annihilation through a light mediator ϕ for 15 nearby dSphs. A combined analysis on the p-wave Sommerfeld enhanced DM annihilation in CR positron excess, DM thermal relic density, gamma-ray constraints from dSphs and CMB constraints is performed. We find that a consistent explanation for all these observables is possible in this scenario.

Note that the gamma-ray observations from other regions of the sky can also place strin-

gent constraints on the DM annihilation, such as that from the Galactic center (GC) observed by H.E.S.S. [54], and the isotropic gamma ray background (IGRB) measured by Fermi-LAT [55]. However, these constraints involve additional uncertainties. As shown in Ref. [56], changing the DM density profile in the Galactic halo from a cusped NFW or Einasto profile to a cored NFW or Einasto profile for a core radius of 500 pc would result in the limits on the DM annihilation cross section to be around two orders of magnitude weaker. A larger core radius would lead to weaker H.E.S.S. constraints. A significant uncertainty in constraining DM properties from IGRB arises from the modeling of the expected DM annihilation luminosity, which depends on the history of DM formation at very large scales. Base on the Millennium II (MS-II) N-body simulation of cosmic structure formation [57], the constraints on DM annihilation from IGRB signals in several scenarios of the expected DM annihilation luminosity was discussed in Ref. [58]. The results showed that the limits in the scenario with only the DM signals from halos/subhalos resolved in MS-II (with mass $\gtrsim 10^6 M_\odot$, where $M_\odot$ is the mass of the Sun) considered are about three orders of magnitude weaker than that in the scenario where a extrapolation of the contribution from halos and subhalos down to $\sim 10^{-6} M_\odot$ was adopted. Note a very large N-body simulation with a high-resolution particle mass of $\sim 10^{-11} M_\odot$ by using a multi-zoom technique was recently completed [59]. It is possible that with higher resolution simulations, the uncertainties from the modeling of the expected DM annihilation luminosity can be reduced. Due to the still large uncertainties in the DM distribution at galactic and cosmological scales, we do not consider these constraints in the present work.

This paper is organized as follows. In Sec. II, we perform an updated analysis on the AMS-02 CR positron data in DM annihilation scenario, and derive the favored DM masses and annihilation cross sections. In Sec. III, we numerically calculate the p-wave Sommerfeld enhancement factors and compare them with the approximate analytic results in the literature. In Sec. IV, the constraints from DM thermal relic density is discussed. In Sec. V, we calculate upper limits on DM annihilation cross section from Fermi-LAT gamma-ray data of 15 nearby dSphs. In Sec. VI, we discuss the constraints from CMB measured by Planck. In Sec. VII, we perform a numerical scan and identify the parameter regions which can explain all the relevant observations. We summarize the conclusions of this work in Sec. IX.

II. AMS-02 POSITRON EXCESS AND DM ANNIHILATION INTERPRETATIONS

In recent years, an excess of CR positron flux at energy above ~ 10 GeV has been observed by a number of experiments including PAMELA [2], Fermi-LAT [3] and AMS-02 [4], which can be possibly related to DM annihilation [12–17, 60]. In this section, we use the CR positron flux data measured by AMS-02 to place constraints on the DM annihilation cross sections. The propagation of CR particles in the Galactic halo can be modeled by a diffusion

process within a diffusion zone which is a cylinder with radius $R_h = 20$ kpc and half-height $Z_h = 1 \sim 10$ kpc. The diffusion equation of CR charged particles is given by [61, 62]

$$\frac{\partial \psi}{\partial t} = \nabla \left(D_{xx} \nabla \psi - \mathbf{V}_c \psi \right) + \frac{\partial}{\partial p} p^2 D_{pp} \frac{\partial}{\partial p} \frac{1}{p^2} \psi - \frac{\partial}{\partial p} \left[\dot{p} \psi - \frac{p}{3} \left(\nabla \cdot \mathbf{V}_c \right) \psi \right] - \frac{1}{\tau_f} \psi - \frac{1}{\tau_r} \psi + q(\mathbf{r}, p) \ , \tag{1}$$

where $\psi(\mathbf{r}, p, t)$ is the CR particle's number density per unit momentum. The spatial diffusion coefficient D_{xx} can be written as $D_{xx} = \beta D_0 (R/R_0)^{\delta}$, where $R = p/(Ze)$ is the rigidity of CR particles with electric charge Ze, $\beta = v/c$ is the velocity of CR particles, D_0 is a normalization constant, δ is the spectral power index, and R_0 is a reference rigidity. $\mathbf{V}_c$ is the convection velocity. $D_{pp} = 4p^2 V_a^2 / (3 D_{xx} \delta (4 - \delta^2)(4 - \delta))$ is the diffusion coefficient in momentum space, where V_a is the Alfvèn velocity which characterizes the propagation of weak disturbances in a magnetic field. $\dot{p} \equiv dp/dt$ is the momentum loss rate of CR particles in propagation. τ_f and τ_r are the time scales of particle fragmentation and radioactive decay respectively. The source term of primary CR particles can be written as $Q(\mathbf{r}, p, t) = f(\mathbf{r}, t) q(p)$, where $f(\mathbf{r}, t)$ is the spatial distribution taken from [63], and $q(p)$ is the momentum distribution. The spectrum of momentum distribution is assumed to be a broken power law in rigidity R, $q(p) \propto (R/R_s)^{\gamma_p}$ with the spectral index $\gamma_p = \gamma_{p1} (\gamma_{p2})$ for the nucleus rigidity R below (above) a reference rigidity R_s. The boundary conditions are that the number density of CR particles vanishes at $r = R_h$ and $z = \pm Z_h$. A steady-state solution can be obtained by setting $\partial \psi / \partial t = 0$. We use the public code `GALPROP v54` [64–68] to numerically solve this propagation equation. We consider a number of propagation models listed in Tab. I. These models are obtained from a global fit to the AMS-02 proton and B/C data using the `GALPROP` code, which represent the typically minimal ("MIN"), median ("MED"), and maximal ("MAX") CR fluxes in re-acceleration (DR) propagation model [17]. We shall focus on the "MED" propagation model as a benchmark model.

Model	R_h (kpc)	Z_h (kpc)	D_0 ($\times 10^{28}$ cm^2 s^{-1})	R_0 (GV)	δ	V_a (km s^{-1})	R_s (GV)	γ_{p1}/γ_{p2}
MIN	20	1.8	3.53	4.0	0.3	42.7	10.0	1.75/2.44
MED	20	3.2	6.50	4.0	0.29	44.8	10.0	1.79/2.45
MAX	20	6.0	10.6	4.0	0.29	43.4	10.0	1.81/2.46

TABLE I: Parameters in the "MIN", "MED" and "MAX" propagation models derived from Ref. [17].

The secondary CR positrons are produced from the interaction of primary CR particles with the interstellar gas. The corresponding source term is given by

$$Q_{\rm sec}(p) = \sum_{i={\rm H,He}} n_i \sum_j \int c \beta_j n_j (p') \frac{d\sigma_{ij}(p, p')}{dp} dp' \ , \tag{2}$$

where n_i is the number density of the interstellar gas, $n_j(p')$ is the number density of CR particles, $d\sigma_{ij}(p, p')/dp$ is the differential cross section for the production of CR positrons.

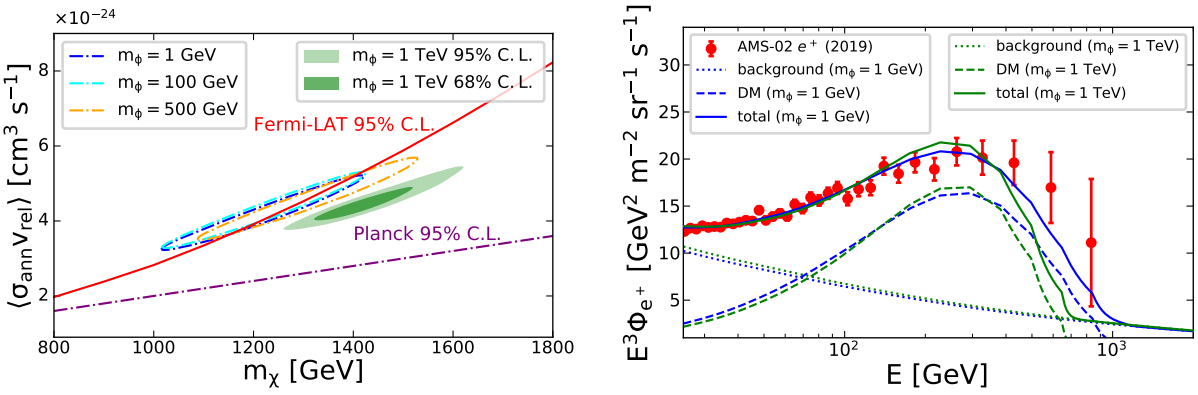


FIG. 1: Left) Regions of DM mass and annihilation cross section favored by the AMS-02 positron flux data [4] for the annihilation channel of $\chi\chi \to 2\phi \to 4\mu$. The green contours correspond to the heavy mediator case with $m_\phi = 1$ TeV, favored by AMS-02 positron data at 95% C.L. (outer) and 68% C.L. (inner). The blue, cyan and orange lines are for the cases with mediator masses $m_\phi = 1$, 100, and 500 GeV, respectively. The red and purple curves stand for upper limits at 95% C.L. derived from the Fermi-LAT data on dSphs gamma rays [21] and the Planck measurements of CMB [1] in the assumption of constant (velocity-independent) DM annihilation cross section. See text for detailed explanation. Right) Best-fit CR positron fluxes (solid lines) for two different mediator masses. The dash and dot curves represent the contributions from DM annihilation and secondary positron backgrounds, respectively. The blue and green curves correspond to mediator masses of m_ϕ=1 GeV and 1 TeV, respectively.

The source term of the primary CR positrons produced by DM self-annihilation in the Galactic halo can be written as

$$q_{e^+}(\mathbf{r}, p) = \frac{\rho_\chi^2(\mathbf{r})\langle\sigma_{\rm ann} v_{\rm rel}\rangle}{2m_\chi^2}\frac{dN_{e^+}}{dp} \ , \tag{3}$$

where ρ_χ is the DM energy density, m_χ is the DM mass, $\langle\sigma_{\rm ann} v_{\rm rel}\rangle$ is the velocity-weighted DM annihilation cross section, and dN_{e^+}/dp is the momentum distribution of positrons. The spatial distribution of DM energy density ρ_χ in the Galactic halo is taken from the Einasto profile [69]

$$\rho_\chi(r) = \rho_\odot \exp\left[-\left(\frac{2}{\alpha_E}\right)\left(\frac{r^{\alpha_E} - r_\odot^{\alpha_E}}{r_s^{\alpha_E}}\right)\right] \ , \tag{4}$$

with $\rho_\odot = 0.43$ GeV cm^{-3}, $\alpha_E = 0.17$, $r_s = 20$ kpc, and $r_\odot = 8.5$ kpc [70].

We focus on the DM annihilation process of DM particles χ to 4μ final state through a mediator ϕ with mass m_ϕ, namely, $2\chi \to 2\phi \to 4\mu$.

The scalar mediator can couple dominantly to leptons through mixing with leptophillic Higgs doublets in some variants of the two-Higgs-doublet models [71, 72]. If the mediator mass is smaller enough, the decay channel of $\tau^+\tau^-$ will be kinematically forbidden, and

the $\mu^+\mu^-$ channel can be dominant. There are also flavor specific scenarios which allow the mediator to couple dominantly to muons in a technically natural way [73, 74]. The Monte-Carlo event generator `PYTHIA 8.2` [75] is used to simulate the dN_{e^+}/dp of positron produced by DM annihilation. The DM particle mass m_χ and velocity-weighted annihilation cross section $\langle\sigma_{\rm ann}v_{\rm rel}\rangle$ are free parameters to be determined by the AMS-02 data. In order to take into account of some uncertainties in the secondary positron flux, such as that from the hadronic interactions, the nuclear enhancement factor from the heavy elements, and the interstellar medium density distribution, we allow the calculated fluxes of secondary positrons to vary global with a free factor C_{e^+}, and take it as an extra free parameter. We perform a Bayesian analysis to the data. To efficiently explore the parameter space, we adopt the `MultiNest` sampling algorithm [76–78].

The fit results including posterior means, standard deviations, and best-fit values are summarized in Tab. II, and the regions favored by the AMS-02 data in the parameter space $(m_\chi, \langle\sigma_{\rm ann}v_{\rm rel}\rangle)$ are shown in the left panel of Fig. 1. It shows that $m_\chi \approx 1-1.6$ TeV with $\langle\sigma_{\rm ann}v_{\rm rel}\rangle \approx (3-6)\times10^{-24}$ cm^3 s^{-1} is favored in this configuration. These results confirm our previous analysis in the heavy mediator limit [17]. We considered several different mediator masses from 1 GeV to 1 TeV. The fit results are found to be insensitive to m_ϕ, if $m_\phi \ll m_\chi$. In the left panel of Fig. 1, we also show the upper limits from Fermi-LAT observations on dSphs gamma rays, which are derived by performing a likelihood analysis following the Fermi-LAT collaboration [21] with heavy mediator mass ~ 1 TeV, and constraints from measurement of CMB from Planck [1] at 95% C.L.. The details of constraints will be discussed in Sec. V and VI. It shows that the regions favored by AMS-02 positron data are in strong tension with the constraints from Planck observation on CMB and only marginally compatible with the constraints from Fermi-LAT observations on dSphs gamma rays, which is a known problem for constant DM annihilation cross section. In the right panel of Fig. 1, we show the calculated CR positron flux with best-fit DM parameters, as well as the secondary positron backgrounds for two different mediator masses. As it can be seen from the figure and also Tab. II, the cases of light mediators predict broader spectra, and are in better agreement with the data.

To have an estimation of the uncertainties arising from the CR propagation models, we also perform fits using the "MIN" and "MAX" propagation models listed in Tab. I. We find that changing the propagation models from "MED" to "MIN" ("MAX") model can lead to a rescaling of m_χ and $\langle\sigma_{\rm ann}v_{\rm rel}\rangle$ favored by AMS-02 positron data by a factor of ~ 0.78 (1.62) and ~ 0.89 (1.48), respectively (see appendix A for details). Such a difference does not change the main conclusion of our analysis.

m_ϕ/GeV	$\log_{10}(m_\chi/\mathrm{GeV})$		$\log_{10}(\langle\sigma_{\rm ann}v_{\rm rel}\rangle/\mathrm{cm}^3\ \mathrm{s}^{-1})$		C_{e^+}		χ^2/d.o.f
	Prior range: [1, 4]		Prior range: [-26, -21]		Prior range: [0.1, 10]		
	(Mean, σ)	Best-fit	(Mean, σ)	Best-fit	(Mean, σ)	Best-fit	
1	3.08 ± 0.03	3.08	-23.39 ± 0.04	-23.39	1.61 ± 0.03	1.61	31.06/32
100	3.08 ± 0.03	3.08	-23.38 ± 0.04	-23.38	1.61 ± 0.03	1.61	30.98/32
500	3.11 ± 0.03	3.11	-23.35 ± 0.04	-23.36	1.62 ± 0.03	1.62	30.56/32
1000	3.15 ± 0.02	3.14	-23.35 ± 0.03	-23.36	1.69 ± 0.02	1.69	52.93/32

TABLE II: Prior ranges, posterior means, standard deviations and best-fit values of DM mass, annihilation cross section, and the normalization factor for different mediator masses in the "MED" propagation model. The values of χ^2/d.o.f are also listed as an estimation of the goodness-of-fit.

III. p-WAVE SOMMERFELD ENHANCEMENT OF DARK MATTER ANNIHILATION

The Sommerfeld enhancement of DM annihilation cross section occurs when the annihilating DM particles self-interact through a long-range attractive potential formed by multiple-exchange of light mediator particles [29]. In this case, the short-distance annihilation cross section can be enhanced as the wave functions of the annihilating particles at origin are distorted from plane wave. When a fermionic DM particle χ couples to a light scalar mediator ϕ, the induced attractive potential is a Yukawa potential $V_Y(\boldsymbol{r}) = -\alpha e^{-m_\phi r}/r$, where m_ϕ is the mass of the mediator, and $\alpha = g^2/4\pi$ is the coupling constant. The two-body wave function $\Psi(\boldsymbol{r})$ of the annihilating DM particles satisfies the following non-relativistic Schrödinger equation

$$-\frac{1}{m_\chi}\nabla^2\Psi(\mathbf{r}) + V_Y(\mathbf{r})\Psi(\mathbf{r}) = m_\chi v^2\Psi(\mathbf{r}) \ , \tag{5}$$

where $v = v_{\rm rel}/2$ is the velocity of DM particles in the center-of-mass frame and $v_{\rm rel}$ is the DM relative velocity. The wave function can be expanded over angular momentum ℓ, namely, $\Psi(r,\theta) = \sum_\ell P_\ell(\cos\theta)\chi_\ell(r)/r$, where P_ℓ is the Legendre polynomial and $\chi_\ell(r)$ is the radial wave function. Adopting the dimensionless parameters $\epsilon_v = v/\alpha$, $\epsilon_\phi = m_\phi/(\alpha m_\chi)$ and rescaling the radial coordinate r with $x = \alpha m_\chi r$, the Schrödinger equation for the radial wave functions $\chi_\ell(x)$ can be written as

$$\chi_\ell''(x) + \left[\epsilon_v^2 - V_\ell(x) - V_Y(x)\right]\chi_\ell(x) = 0 \ , \tag{6}$$

where $V_\ell(x) = \ell(\ell+1)/x^2$ is the centrifugal potential, and $V_Y(x) = -e^{-\epsilon_\phi x}/x$ is the Yukawa potential in terms of x. Eq. (6) should be solved with the following boundary conditions [36, 37]

$$\lim_{x\to 0}\chi_\ell(x) = (\epsilon_v x)^{\ell+1} \ , \text{ and } \lim_{x\to\infty}\chi_\ell(x) \to C_\ell \sin\left(\epsilon_v x - \frac{\ell\pi}{2} + \delta_\ell\right) \ , \tag{7}$$

where C_ℓ is a normalization constant, and δ_ℓ is the phase shift of the ℓ-th partial wave. The Sommerfeld enhancement factor for the ℓ-th partial wave is defined as [33]

$$S_\ell^Y \equiv \lim_{x\to 0}\left|\frac{\chi_\ell(x)}{\chi_\ell^{(0)}(x)}\right|^2 = \left[\frac{(2\ell+1)!!}{C_\ell}\right]^2 , \tag{8}$$

where $\chi_\ell^{(0)}(x)$ is the ℓ-th radial wave function which is the solution of the Schrödinger equation in the absence of a potential.

Approximate analytic solutions can be obtained by approximating the Yukawa potential with the Hulthén potential [37, 79]

$$V_Y(x) \approx V_H(x) = -\frac{\delta e^{-\delta x}}{1-e^{-\delta x}} , \tag{9}$$

where $\delta = \pi^2\epsilon_\phi/6$. In this approximation, the s-wave Sommerfeld enhancement factor S_0^H has the well-known form [79]

$$S_0^H = \frac{\pi}{\varepsilon_v}\frac{\sinh\left(\frac{2\pi\varepsilon_v}{\pi^2\varepsilon_\phi/6}\right)}{\cosh\left(\frac{2\pi\varepsilon_v}{\pi^2\varepsilon_\phi/6}\right)-\cos\left(2\pi\sqrt{\frac{1}{\pi^2\varepsilon_\phi/6}-\frac{\varepsilon_v^2}{\left(\pi^2\varepsilon_\phi/6\right)^2}}\right)} . \tag{10}$$

The s-wave Sommerfeld enhancement factor has two important characters. One is that the Sommerfeld enhancement saturates at low velocity, once the deBroglie wavelength of the incident particle gets larger than the range of interaction, equivalently, $\epsilon_v \ll \epsilon_\phi$. The other is the additional resonant enhancement from the threshold bound states developed by the attractive potential for specific values of $\epsilon_\phi \simeq 6/(n^2\pi^2)$, $(n = 1, 2, 3\ldots)$. In the case of s-wave annihilation, the centrifugal potential vanishes and the Hulthén potential can approximate the Yukawa potential very well. Thus Eq. (10) is an excellent approximation of S_0^Y, which typically reproduces the numerical results with uncertainties less than $\sim 10\%$, and accurately reproduces the resonant behavior [41].

For higher partial waves with $\ell \neq 0$, in order to obtain approximate analytic expressions, additional approximation has to be applied to the centrifugal potential [37]

$$V_\ell(x) \approx \tilde{V}_\ell(x) = \ell(\ell+1)\frac{\delta^2 e^{-\delta x}}{(1-e^{-\delta x})^2} . \tag{11}$$

Under this approximation, the analytic expression of the p-wave Sommerfeld enhancement factor is given by [79]

$$S_1^H = \frac{(1-\varepsilon_\phi\pi^2/6)^2+4\varepsilon_v^2}{(\varepsilon_\phi\pi^2/6)^2+4\varepsilon_v^2}S_0^H . \tag{12}$$

Although this approximation is reasonable at short distances with $\delta\cdot x \ll 1$, it does not well reproduce the long-distance behavior of $V_\ell(x)$. In the left panel of Fig. 2, we show the difference between $V_H(x)+\tilde{V}_{\ell=1}(x)$ and $V_Y(x)+V_{\ell=1}(x)$. It can be seen that the difference

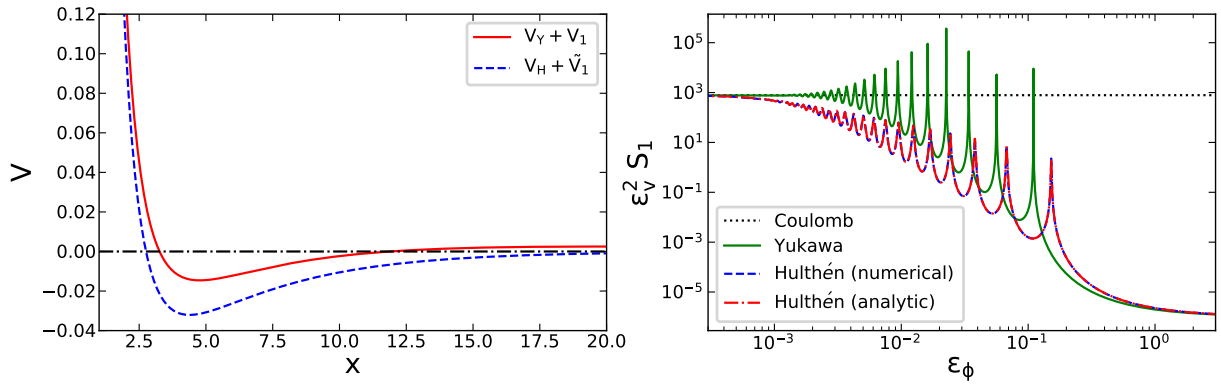


FIG. 2: Left) Comparison between the Yukawa potential plus the centrifugal potential $V_Y(x) + V_{\ell=1}(x)$ and the Hulthén potential plus the approximate centrifugal potential $V_H(x) + \tilde{V}_{\ell=1}(x)$ as a function of x with ϵ_ϕ fixed at $= 6/(2^2\pi^2)$. Right) Values of the rescaled p-wave Sommefeld enhancement factor $\epsilon_v^2 S_1^Y$ as a function of ϵ_ϕ at fixed $\epsilon_v = 10^{-3}$. The green solid line represents the numerical solution for Yukawa potential, the red dashed line is the approximate analytic result for Hulthén potential, the blue dashed line stands for the numerical result for Hulthén potential as a comparison. The black dot line corresponds to the Coulomb limit.

becomes significant near the force-range of the Yukawa and Hulthén potentials, i.e., $\sim 1/\epsilon_\phi$. For this reason, Eq. (12) is not a reasonable approximation for p-wave process due to the mismatch of the two potentials, especially near the resonant regions. We directly calculate the p-wave Sommerfeld enhancement factors for Yukawa potential from numerically solving Eq. (6). Since the p-wave annihilation cross section before the enhancement is proportional to $v_{\rm rel}^2$, we show the rescaled enhancement factor $\epsilon_v^2 S_1^Y$ calculated numerically from the Schrödinger equation and $\epsilon_v^2 S_1^H$ calculated using Eq. (12) in the right panel of Fig. 2. As the figure shows, the difference between the two method is significant. In general, the direct numerical calculation for the Yukawa potential gives significantly larger enhancement factor and different locations of the resonance, which may have important phenomenological consequences. For an estimation of the accuracy of the numerical solutions, we numerically solve the Sommerfeld enhancement factors for the Hulthén potential case and compare them with the analytic solutions. We find an excellent agreement between the two methods, which is also shown in Fig. 2. Therefore, we shall adopt the numerical values of p-wave Sommerfeld enhancement factor S_1^Y in this work.

The fact that the Hulthén-potential approximation cannot well reproduce the p-wave Sommerfeld enhancement factors induced by the Yukawa potential may have important phenomenological implications. For the Hulthén potential, as shown in Eq. (12), the values of ϵ_ϕ at the resonance points are the same for both the s- and p-wave cases. Our direct numerical calculations indicate that this is in general *not true* for the the Yukawa potential. In the generic case, DM annihilation can involve both s- and p-wave processes. Due to the

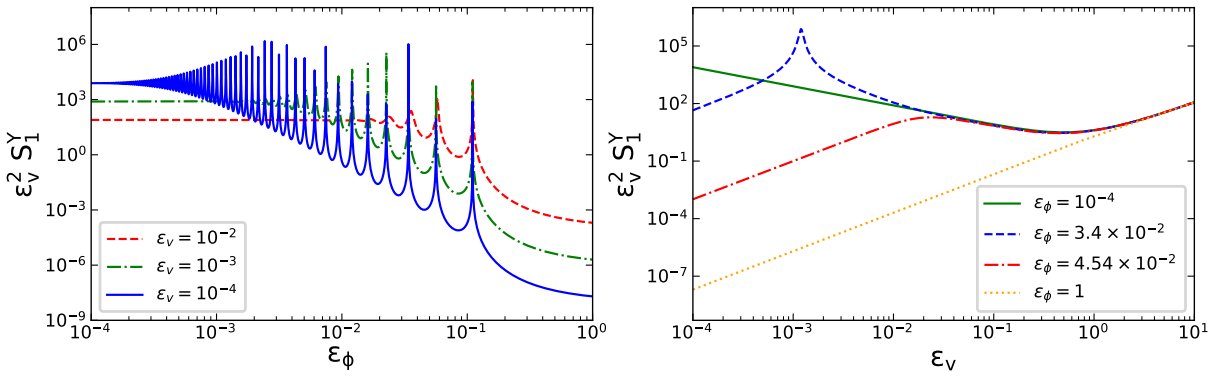


FIG. 3: Left) p-wave Sommefeld enhacement factor $\epsilon_v^2 S_1^Y$ as a function of ϵ_ϕ with $\epsilon_v = 10^{-2},\ 10^{-3}$, and 10^{-4}, respectively. Right) $\epsilon_v^2 S_1^Y$ as a function of ϵ_v with $\epsilon_\phi = 10^{-4},\ 3.4 \times 10^{-2},\ 4.54 \times 10^{-2}$, and 1.0, respectively.

different locations of the resonance points, the s- and p-wave Sommerfeld enhancement will not reach the resonance point simultaneously. Thus it is possible that for a given parameter set, only the p-wave or s-wave Sommerfeld enhancement is significant.

Another major difference from the s-wave case is that the p-wave Sommerfeld-enhanced annihilation cross section can be both velocity-enhanced (for $\epsilon_v \gg \epsilon_\phi$) and velocity-suppressed (for $\epsilon_v \ll \epsilon_\phi$), which is also important in phenomenology. In the left panel of Fig. 3, we show the value of $\epsilon_v^2 S_1^Y$ as a function of the dimensionless parameter ϵ_ϕ for three typical value of $\epsilon_v = 10^{-2}, 10^{-3}$, and 10^{-4}, respectively. It shows that $\epsilon_v^2 S_1^Y$ is higher (lower) at lower ϵ_v for $\epsilon_\phi \ll \epsilon_v$ ($\epsilon_\phi \gg \epsilon_v$). In the right panel of Fig. 3, we show the dependence of $\epsilon_v^2 S_1^Y$ on dimensionless parameters ϵ_v for four typical values of $\epsilon_\phi = 10^{-4}, 3.4 \times 10^{-2}, 4.54 \times 10^{-2}$, and 1.0. The value of 3.4×10^{-2} (4.54×10^{-2}) is a representative value for ϵ_ϕ which is on (off) the resonance region. For $\epsilon_\phi \gtrsim 1$ or $\epsilon_v \gtrsim 1$, there is no Sommerfeld enhancement, $S_1^Y \sim 1$, thus $\epsilon_v^2 S_1^Y$ scales as ϵ_v^2. For $\epsilon_\phi \lesssim \epsilon_v \lesssim 1$, S_1^Y approaches the Coulomb limit, hence $\epsilon_v^2 S_1^Y$ scales as $1/\epsilon_v$. For $\epsilon_v \lesssim \epsilon_\phi \lesssim 1$, when the effect of the Sommerfeld enhancement is not saturated, $\epsilon_v^2 S_1^Y$ scales as $1/\epsilon_v^2$ near the resonance regions and $1/\epsilon_v$ away from the resonance regions. Once S_1^Y has saturated ($\epsilon_\phi \gg \epsilon_v$), S_1^Y remains the same and $\epsilon_v^2 S_1^Y$ scales as ϵ_v^2. It is possible that the complicated velocity dependence may allow the p-wave Sommerfeld enhancement to accommodate the data of DM relic density, AMS-02 positron flux, gamma rays of dSphs, and CMB simultaneously.

IV. CONSTRAINTS FROM THERMAL RELIC DENSITY

The time (thermal) evolution of the DM number density n is governed by the Boltzmann equation [80]

$$\frac{dn}{dt} + 3H(t)n = -\left\langle \sigma_{\rm ann} v_{\rm rel} \right\rangle \left(n^2 - n_{eq}^2 \right) \ , \tag{13}$$

where $H(t)$ is the Hubble parameter, n_{eq} is the DM number density in equilibrium. Changing variables from $t \to x = m_\chi/T$, $n \to Y = n/s$ and $n_{eq} \to Y_{eq} = n_{eq}/s$, where T is the temperature of thermal bath and s is the entropy density, the Boltzmann equation can be rewritten as [81]

$$\frac{dY}{dx} = -\sqrt{\frac{\pi}{45}} m_{\rm pl} m_\chi g_*^{-1/2} g_{*s} x^{-2} \langle \sigma_{\rm ann} v_{\rm rel} \rangle \left(Y^2 - Y_{eq}^2 \right) \ , \tag{14}$$

where $m_{\rm pl} \simeq 1.22 \times 10^{19}$ GeV is the Planck mass scale, g_* and g_{*s} are the effective relativistic degrees of freedom for energy and entropy density, respectively [82]. In a p-wave Sommerfeld enhanced DM annihilation model, the annihilation cross section is $\sigma_{\rm ann} v_{\rm rel} = (\sigma_{\rm ann} v_{\rm rel})_0 \times S_1$, where $(\sigma_{\rm ann} v_{\rm rel})_0 = b v_{\rm rel}^2$ is the short-distance cross section and b is a global factor. If the DM particles are in thermal equilibrium, the velocity distribution function $f(v)$ of DM particles is the Maxwell-Boltzmann distribution

$$f(v) = \left(\frac{1}{\pi v_0^2} \right)^{3/2} e^{-\frac{v^2}{v_0^2}} \ , \tag{15}$$

with v_0 the most probable velocity. The velocity-weighted annihilation cross section with the Sommerfeld enhancement is given by

$$\langle \sigma_{\rm ann} v_{\rm rel} \rangle = \frac{b}{v_0^3} \sqrt{\frac{2}{\pi}} \int_0^{+\infty} {\rm d}v_{\rm rel} e^{-\frac{v_{\rm rel}^2}{2v_0^2}} v_{\rm rel}^4 S_1(v_{\rm rel}/2\alpha, \epsilon_\phi) \ . \tag{16}$$

The velocity-weighted DM annihilation cross section is assumed to be in the form of Eq. (16) with $v_0 = \sqrt{2T_\chi/m_\chi}$, where T_χ is the temperature of DM particles. If the DM particles are in equilibrium with the thermal bath, $T_\chi = T$.

The relic abundance of DM particles can be written as [83]

$$\Omega_\chi h^2 \approx 2.76 \times 10^8 Y(x_\infty) \left(\frac{m_\chi}{\rm GeV} \right) \ , \tag{17}$$

where x_∞ is the value of x in the present day. The observed value of DM relic abundance from Planck is $\Omega_\chi h^2 \simeq 0.1193$ [1]. We numerically solve the Boltzmann equation of Eq. (14) with the Sommerfeld-enhanced DM annihilation cross section. During the calculation we have assumed that the mediator particles are in thermal equilibrium at freeze-out of DM particles. As shown in [83], although the effect of kinetic decoupling in s-wave process reduces DM relic abundance significantly, the kinetic decoupling effect in Sommerfeld enhanced p-wave annihilation is negligible, if the DM freeze-out temperature T_f is higher than kinetic decoupling temperature $T_f/T_{\rm kd} \gtrsim \mathcal{O}(1)$, which is easily satisfied. We thus do not consider the kinetic decoupling in this work, namely, the relation $T_\chi \approx T$ is assumed.

With the requirement that the observed DM relic abundance $\Omega_\chi h^2$ must be reproduced, the value of b in the expression of DM annihilation cross section can be determined for given parameters α, m_χ and m_ϕ. Using the determined value of b, the p-wave annihilation cross section $\langle \sigma_{\rm ann} v_{\rm rel} \rangle$ can be predicted from Eq. (16), for a given velocity distribution

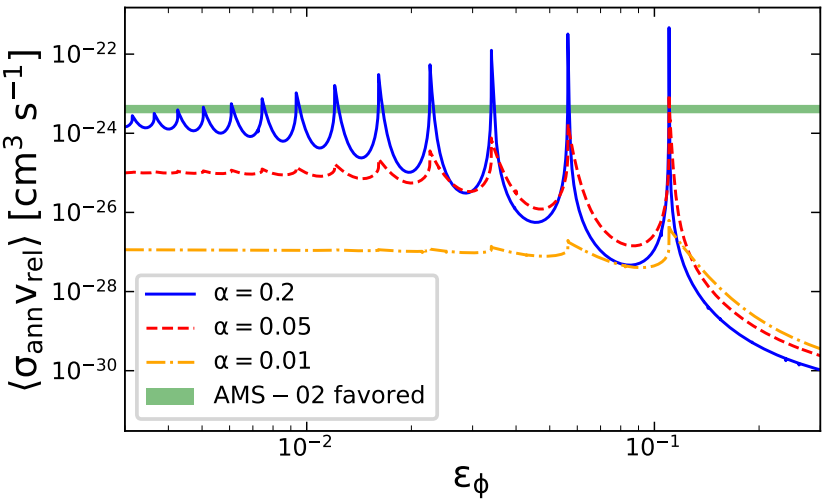


FIG. 4: $\langle\sigma_{\rm ann}v_{\rm rel}\rangle$ calculated from Eq. (16) with $v_0 = 220$ km s^{-1} as a function of ϵ_ϕ for $\alpha = 0.01,\ 0.05$, and 0.2, where DM mass is fixed at the best-fit value of AMS-02 positron data $m_\chi = 1.2$ TeV and b is derived from the correct DM relic density. The green area is favored by AMS-02 positron data [4] at 95% CL with $m_\phi = 1$ GeV for 4μ channel in "MED" propagation model.

characterized by the most probable velocity v_0. In the Galactic halo $v_0 = v_{\rm halo} \approx 220$ km s^{-1}. In Fig. 4, we show the predicted value of $\langle\sigma_{\rm ann}v_{\rm rel}\rangle_{v_{\rm halo}}$ as a function of ϵ_ϕ after the constraints from the DM thermal relic density, for three typical values of $\alpha = 0.2,\ 0.05$, and 0.01, respectively. The DM mass is fixed at the best-fit value of AMS-02 positron data, $m_\chi = 1.2$ TeV and the mediator mass is fixed at $m_\phi = 1$ GeV. The figure shows that in general a large coupling constant $\alpha \gtrsim 0.1$ is needed to achieve a large enough DM annihilation cross section to explain the AMS-02 positron data.

A large α may lead to large annihilation cross section for the process of $\chi\chi \to 2\phi$ which will also be subjected to the constraints from DM thermal relic density [41, 49]. This kind of constraint is, however, model dependent. It is possible to have α at the scale of $\mathcal{O}(10^{-1})$ in some well-motivated DM models. For instance, in the case when the interaction Lagrangian has the form $\mathcal{L}_{\rm int} = -g\chi\chi\phi/2 - \mu\phi^3/3!$, where $g = \sqrt{4\pi\alpha}$, the annihilation $\chi\chi \to \phi\phi$ is a p-wave process with tree-level cross section [40]

$$(\sigma_{\rm ann}v_{\rm rel})_0 = \kappa\frac{3\pi\alpha^2}{8m_\chi^2}v_{\rm rel}^2 \tag{18}$$

with $\kappa = 1 - 5\xi/18 + \xi^2/48$, where $\xi = \mu/(m_\chi g)$ [83]. The global factor b has the form $b = 3\pi k\alpha^2/(8m_\chi^2)$. Using an approximate analytic solution to the Boltzmann equation Eq. (14) in which the Sommerfeld enhancement is neglected due to the high velocity of DM particles at freeze-out, the requirement from the correct thermal cross section is [80, 84]

$$\frac{6b}{x_f} \approx 3 \times 10^{-26}\ {\rm cm}^3\ {\rm s}^{-1}\ , \tag{19}$$

where $x_f \sim 20$ is the value of x at freeze-out. Hence the scale of the coupling constant α is estimated as

$$\alpha \sim 0.25 \left(\frac{0.1}{k}\right)^{\frac{1}{2}} \left(\frac{m_\chi}{1\ \mathrm{TeV}}\right) \ . \tag{20}$$

In the case of cubic self-interaction, the minimum value of k is 2/27, which can lead to $\alpha \sim 0.3\,(m_\chi/1\ \mathrm{TeV})$. We thus set set the benchmark value of $\alpha \approx 0.2$ in this work.

V. CONSTRAINTS FROM FERMI-LAT GAMMA-RAY OBSERVATIONS OF DWARF SPHEROIDAL SATELLITE GALAXIES

The dSphs are particularly promising targets for DM indirect detection due to their low diffuse Galactic gamma-ray backgrounds and high DM density [85]. The gamma-ray flux from DM self-annihilation within an energy range ($E_{\rm min}$, $E_{\rm max}$) from a solid angle $\Delta\Omega$ is given by

$$\begin{aligned}\Phi_\gamma(\Delta\Omega, E_{\rm min}, E_{\rm max}) =& \frac{1}{8\pi m_\chi^2} \int_{E_{\rm min}}^{E_{\rm max}} \frac{dN_\gamma}{dE_\gamma} dE_\gamma \\ & \times \int_{\Delta\Omega} d\Omega \int_{\rm l.o.s} dl \int d^3\boldsymbol{v}_1 \int d^3\boldsymbol{v}_2 f\left(\boldsymbol{r}, \boldsymbol{v}_1\right) f\left(\boldsymbol{r}, \boldsymbol{v}_2\right) \left(\sigma_{\rm ann} v_{\rm rel}\right) \ ,\end{aligned} \tag{21}$$

where $f\left(\boldsymbol{r}, \boldsymbol{v}\right)$ is the DM phase-space distribution function. In the cases where the velocity-dependence of $\sigma_{\rm ann} v_{\rm rel}$ can be factorized out, the gamma-ray flux can be written as

$$\Phi_\gamma(\Delta\Omega, E_{\rm min}, E_{\rm max}) = \frac{C}{8\pi m_\chi^2} \int_{E_{\rm min}}^{E_{\rm max}} \frac{dN_\gamma}{dE_\gamma} dE_\gamma \times J, \tag{22}$$

where C is a velocity-independent part of the annihilation cross section and the J-factor contains the information of DM density distribution and the velocity-dependent part of the cross section. For instance, in the simplest case where $\sigma_{\rm ann} v_{\rm rel}$ is velocity independent. $C = \sigma_{\rm ann} v_{\rm rel}$ and the corresponding J-factor is

$$J_0 = \int_{\Delta\Omega} d\Omega \int_{\rm l.o.s} \rho^2(\mathbf{r}) dl \ , \tag{23}$$

The J_0-factor encapsulates purely the astrophysical information, which contains a line-of-sight (l.o.s) integral through the square of DM distribution $\rho(\mathbf{r})$ over a slolid angle $\Delta\Omega$. In the case of s-wave Sommerfeld-enhanced DM annihilation, $C = (\sigma_{\rm ann} v_{\rm rel})_0$ and the J-factor becomes

$$J_s = \int_{\Delta\Omega} d\Omega \int_{\rm l.o.s} dl \int d^3\boldsymbol{v}_1 \int d^3\boldsymbol{v}_2 f\left(\boldsymbol{r}, \boldsymbol{v}_1\right) f\left(\boldsymbol{r}, \boldsymbol{v}_2\right) S_0(v_{\rm rel}). \tag{24}$$

The integration over the DM velocity should be cut off at the escape velocity $v_{\rm esc}$ for a given dSph. Similarly, in the case of p-wave Sommerfeld-enhanced DM annihilation, $C = b$ and the corresponding J-factor is

$$J_p = \int_{\Delta\Omega} d\Omega \int_{l.o.s} dl \int d^3\boldsymbol{v}_1 \int d^3\boldsymbol{v}_2 f\left(\boldsymbol{r}, \boldsymbol{v}_1\right) f\left(\boldsymbol{r}, \boldsymbol{v}_2\right) v_{\rm rel}^2 S_1(v_{\rm rel}). \tag{25}$$

In this section, we investigate how the p-wave Sommerfeld enhancement affects the J-factors for dSphs and derive the constraints on DM annihilation from Fermi-LAT data on gamma rays from dSphs. We will consider 15 dSphs in the combined analysis of Fermi-LAT collaboration [21] which are listed in Table. III. They are selected from 18 dSphs with kinematically determined J-factors. Three of these 18 dSphs, Canes Venatici I, Leo I and Ursa Major I are excluded to ensure statistical independence between observations, since they overlap with other dSphs.

A. DM velocity distribution within dSphs

In the case of velocity-dependent DM annihilation cross sections, the gamma-ray flux arising from DM annihilation depends also on the DM velocity distribution within dSphs. To determine the DM velocity distribution function, we adopt a simple assumption that the gravitation potential of dSphs is spherically-symmetric and the velocity distribution of DM particles is isotropic. In this case, the isotropic distribution function of DM particles with a given energy density profile $\rho_\chi(r)$ in dSphs can be determined by the Eddington's formula [86]

$$f_\chi(\epsilon) = \frac{1}{\sqrt{8}\pi^2}\int_\epsilon^0 \frac{d^2\rho}{d\Psi^2}\frac{d\Psi}{\sqrt{\Psi-\epsilon}}\ , \tag{26}$$

where Ψ is the spherical-symmetric gravitational potential, and ϵ is the gravitational binding energy per mass of a DM particle. The function $f_\chi(\epsilon)$ is essentially the DM phase-space distribution $f_\chi(r,v)$, as $\epsilon = v^2/2 + \Psi(r)$ is implicitly a function of both v and r. In this work, the density profile of DM particles in dSphs is assumed to be the Navarro-Frenk-White (NFW) profile [87]

$$\rho_\chi(r) = \frac{\rho_s}{(r/r_s)\,(1+r/r_s)^2}\ , \tag{27}$$

where the parameters ρ_s and r_s are the reference density and radius, respectively. The two parameters can be determined by the maximum circular velocity $V_{\rm max}$ and the radius of maximum circular velocity $R_{V_{\rm max}}$ of the dSph through the relations

$$r_s = \frac{R_{V_{\rm max}}}{2.163}\ ,\ \text{and}\ \rho_s = \frac{4.625}{4\pi G}\left(\frac{V_{\rm max}}{r_s}\right)^2. \tag{28}$$

Thus, the DM distribution function $f_\chi(r,v)$ depends only on the astrophysical parameters $(V_{\rm max}, R_{V_{\rm max}})$, which can be determined by the observation of the average stellar line-of-sight velocity dispersion of each dSph.

In Fig. 5, we show the velocity distribution rescaled by v^2 calculated from Eq. (26) $v^2 f(r,v)$ at radius $r = r_s/2$ as a function of v for a selection of four typical dSphs, Canes Venatici II, Ursa Minor, Sculptor, and Leo IV selected from the 15 dSphs. The values of $(V_{\rm max}, R_{V_{\rm max}})$ for these dSphs are taken from Ref. [88], and the NFW profile parameter (ρ_s, r_s) are determined by Eq. (28). Note that the measured rotation curves of some dSphs

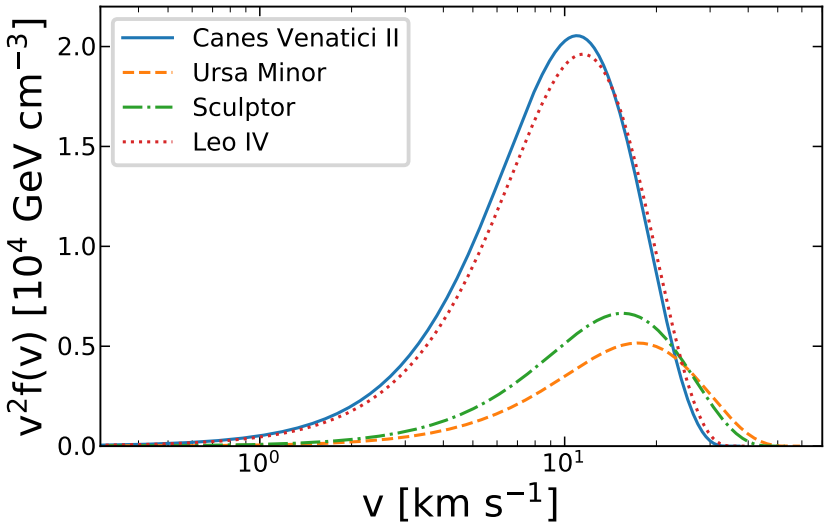


FIG. 5: Velocity distribution functions $v^2 f(v)$ evaluated at radius $r = r_s/2$ using the Eddington's formula [86] for a selection of four dSphs Canes Venatici II, Ursa Minor, Sculptor, and Leo IV.

suggests the cored DM profile [89–91]. Extending the calculations for non-NFW profiles is straightforward. It only requires modifying the relation of Eq. (28) accordingly. The value of $V_{\rm max}$ and $R_{V_{\rm max}}$ of each dSph with other profiles, such as cored NFW, Burkert, and Einasto profile can be found in Ref. [88].

B. p-wave Sommerfeld-enhanced J-factor

Using the isotropic phase-space distribution of DM particles in dSphs of Eq. (26), the expression of J_p can be written as

$$J_p = \frac{32\pi^3}{D^2}\int_0^{r_{\rm max}} r^2 dr \int_0^{v_{\rm esc}(r)} v_1^2 f_\chi\left(r, v_1\right) dv_1 \int_0^{v_{\rm esc}(r)} v_2^2 f_\chi\left(r, v_2\right) dv_2 \\ \times \int_0^{\pi} \sin\theta S_1\left(\sqrt{v_1^2 + v_2^2 - 2v_1 v_2 \cos\theta}/2\alpha, \epsilon_\phi\right)(v_1^2 + v_2^2 - 2v_1 v_2\cos\theta) d\theta \ , \tag{29}$$

where D is the distance from the Solar system to the center of the dSphs under consideration, whose values are taken from Ref. [21]. $v_{\rm esc}(r) = \sqrt{-2\Psi(r)}$ is the escape velocity at radius r. The integral over solid angle is performed over a circular region with a solid angle of $\Delta\Omega \sim 2.4 \times 10^{-4}$ sr, namely, angular radius of $\beta = 0.5^\circ$ which corresponds to the maximal radius $r_{\rm max} = D \cdot \sin\beta$. In the assumption of NFW profile of DM distribution in dSphs, the set of DM halo scale radii r_s span a range of subtended angles between 0.1° and 0.4° [92]. Since $\Delta\Omega$ is large enough to essentially encompass the entire region of the dSphs in which there is significant dark matter annihilation, the J-factor can be expressed in terms of an integral over the radial distance from the center of the dSphs, instead of an integral over

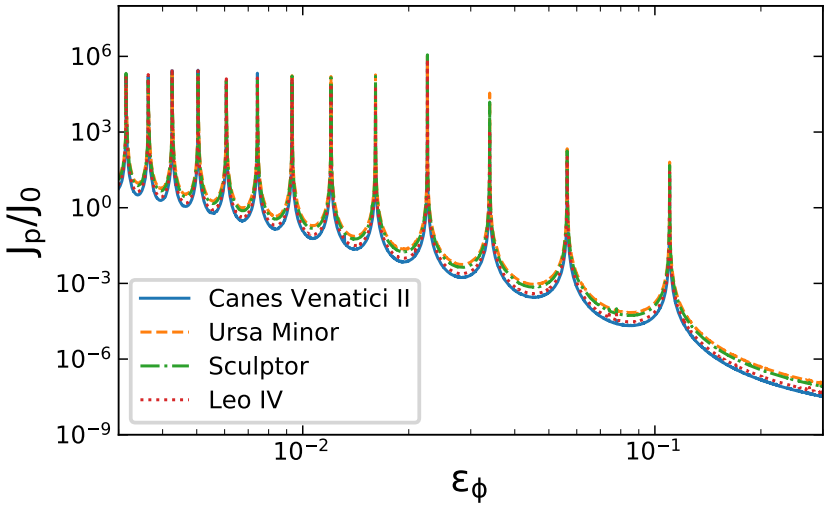


FIG. 6: The ratio of J_p/J_0 as a function of ϵ_ϕ for the four dSphs Canes Venatici II, Ursa Minor, Sculptor, and Leo IV. The value of the coupling strength is fixed at $\alpha = 0.2$.

the line of sight. The value of J_p depends on five parameters: two of them are related to particle physics: α and ϵ_ϕ. Another three are astrophysical parameters: D, $V_{\rm max}$ and $R_{V_{\rm max}}$.

In Fig. 6, we show the ratio between the p-wave Sommerfeld-enhanced J-factor J_p and the normal J-factor J_0 calculated in [21] as a function of ϵ_ϕ for the four dSphs considered in Fig. 5. In Table. III, we list the values of J_p at four typical values of $\epsilon_\phi = 0.005,\ 0.006,\ 0.009,$ and 0.05 for all the fifteen dSphs. Similar to the s-wave Sommerfeld-enhanced J-factor J_s calculated in Ref. [93, 94], J_p has the resonant behavior at certain values of ϵ_ϕ due to the Sommerfeld enhancement factor in Eq. (29). Near the resonant regions, J_p can be a few orders of magnitude larger than J_0. Unlike J_s which is always greater than J_0, the value of J_p can be suppressed at some ϵ_ϕ, where the Sommerfeld enhancement is subdominant compared with the velocity suppression factor $v_{\rm rel}^2$. In the limit of a heavy mediator, there is no Sommerfeld enhancement. Thus J_s/J_0 approaches to 1, while J_p/J_0 approaches to $v_{\rm dSphs}^2$, where $v_{\rm dSphs} \approx 10$ km s^{-1} is the DM typical velocity in dSphs.

In the case of p-wave Sommerfeld enhancement, the dSphs which have similar J_0 factors may have quite different values of J_p. For instance Bootes I and Draco have nearly the same J_0 factor of 6.3×10^{18} GeV^{2}cm^{-5}, but the corresponding J_p factors at $\epsilon_\phi = 0.005$ are 3.1×10^{20} GeV^{2}cm^{-5} and 5.0×10^{20} GeV^{2}cm^{-5}, respectively. This changes the relative importance of J_p among the dSphs in their contribution to the gamma-ray flux. For instance, Ursa Minor and Draco become more important in J_p than they are in J_0. However, Segue 1 (Leo II) remains to be the brightest (faintest) dSph among all the fifteen dSphs.

J_p calculated in this work is based on the assumption of isotropic velocity distribution and NFW profile of DM in dSphs. Extending the calculation of J_p to other DM distributions is straightforward. Due to the low dispersion of DM velocity in dSphs, J_p can be approximately

Name	$J_p(0.005)[\times 10^{20}]$	$J_p(0.006)[\times 10^{19}]$	$J_p(0.009)[\times 10^{18}]$	$J_p(0.05)[\times 10^{15}]$	$J_0[\times 10^{18}]$
Bootes I	3.1	13.3	5.7	4.7	6.3
Canes Venatici II	0.3	1.1	0.4	0.3	0.8
Carina	0.5	2.2	0.9	0.7	1.3
Coma Berenices	3.4	13.9	5.5	4.6	10.0
Draco	5.0	22.2	9.7	8.2	6.3
Fornax	1.1	5.0	2.3	1.9	1.6
Hercules	0.5	1.9	0.8	0.7	1.3
Leo II	0.2	0.7	0.3	0.2	0.4
Leo IV	0.3	1.4	0.6	0.5	0.8
Sculptor	2.8	11.9	5.2	4.4	4.0
Segue 1	11.4	46.1	17.7	14.9	31.6
Sextans	1.4	5.7	2.4	2.0	2.5
Ursa Major II	8.8	35.8	15.1	12.5	20.0
Ursa Minor	5.1	22.8	10.3	9.0	6.3
Willman 1	4.4	18.0	7.3	5.9	12.6

TABLE III: $J_p(\epsilon_\phi)$ (in unit of GeV^2 cm^{-5}) of 15 dSphs at $\epsilon_\phi = 0.005,\ 0.006,\ 0.009$, and 0.05 with $\alpha = 0.2$. The last column shows the values of J_0 from [21].

as $J_p \sim v_{\rm dSphs}^2 S_1(v_{\rm dSphs}) J_0$. It has been shown that J_0 is fairly insensitive to the assumed DM density profile [95, 96], hence J_p is expected to weakly dependent of the DM profile in dSphs.

C. Constraints on DM annihilation cross section from Fermi-LAT dSphs gamma-ray data

We place constraints on the DM annihilation cross sections using six years of Fermi-LAT PASS8 data on gamma rays from the fifteen dSphs listed in Tab. III. The gamma-ray fluxes are measured in the energy range of 500 MeV $-$ 500 GeV, and are binned into 24 logarithmically-spaced bins. The likelihood function for an individual dSph with index i is given by [21]

$$\mathcal{L}_i\left(\boldsymbol{\mu}, \hat{\boldsymbol{\theta}}_i \mid \mathcal{D}_i\right) = \prod_{j=1}^{24} \mathcal{L}_{ij}\left(\boldsymbol{\mu}, \hat{\boldsymbol{\theta}}_i \mid \mathcal{D}_{ij}\right) \ , \tag{30}$$

where $\mathcal{L}_{ij}\left(\boldsymbol{\mu}, \hat{\boldsymbol{\theta}}_i \mid \mathcal{D}_{ij}\right)$ is the likelihood function for the i-th dSph in the j-th energy bin, $\boldsymbol{\mu}$ stands for the parameters of the DM model, $\hat{\boldsymbol{\theta}}_i$ are the best-fit values of the nuisance parameters such as the flux normalizations of background gamma-ray sources, and $\mathcal{D}_{ij}$ represent the observed gamma-ray fluxes. The likelihood as a function of gamma-ray flux is

explicitly given by the Fermi-LAT collaboration in [97]. To determine the constraint on the parameters of a given DM model $\boldsymbol{\mu}$, we adopt the standard delta-log-likelihood approach. We calculate the quantity $\Delta\chi^2(\boldsymbol{\mu})$ as follows

$$\Delta\chi^2(\boldsymbol{\mu}) = -2\ln\left(\frac{\mathcal{L}_i\left(\boldsymbol{\mu}, \hat{\boldsymbol{\theta}}_i \mid \mathcal{D}_i\right)}{\mathcal{L}_i(\hat{\boldsymbol{\mu}}, \hat{\boldsymbol{\theta}}_i \mid \mathcal{D}_i)}\right) , \tag{31}$$

where $\hat{\boldsymbol{\mu}}$ are the values which maximize $\mathcal{L}_i\left(\boldsymbol{\mu}, \hat{\boldsymbol{\theta}}_i \mid \mathcal{D}_i\right)$. The upper limits on the DM parameter $\boldsymbol{\mu}$ at a given m_χ from Fermi-LAT gamma-ray data on dSph i at 95% C.L. are determined by requiring $\Delta\chi^2 \leq 2.71$, if $\boldsymbol{\mu}$ is a one-dimensional quantity. For a combined analysis for all the dSphs, one can replace the individual likelihood function of dSph i $\mathcal{L}_i\left(\boldsymbol{\mu}, \hat{\boldsymbol{\theta}}_i \mid \mathcal{D}_i\right)$ with a joint likelihood function $\mathcal{L}\left(\boldsymbol{\mu}, \hat{\boldsymbol{\theta}} \mid \mathcal{D}\right) = \prod_{i=1}^{15} \mathcal{L}_i\left(\boldsymbol{\mu}, \hat{\boldsymbol{\theta}}_i \mid \mathcal{D}_i\right)$ in the above equation. Note that statistical uncertainties in $V_{\rm max}$ and $R_{V_{\rm max}}$ may affect the J-factor determination [88]. These uncertainties can give rise to the uncertainties of DM density profile in dSphs through Eq. (28), and then the J-factor (with and without Sommerfeld enhancement) through Eq. (23-25). For DM annihilation models with constant cross section, the Fermi-LAT collaboration has incorporated this part of uncertainties in the J_0 determination as a nuisance parameter with an extra likelihood function in Gaussian form [21]. As shown in [94], the upper limits of DM annihilation cross section can be modified by at most $2\%-5\%$ when this part of astrophysical uncertainties is not taken into account. For simplicity, we thus do not consider the uncertainties in $V_{\rm max}$ and $R_{V_{\rm max}}$ in this work.

For DM annihilation models with constant (velocity-independent) cross sections, the parameter set of DM model $\boldsymbol{\mu}$ is simply $\langle\sigma_{\rm ann}v_{\rm rel}\rangle$. The gamma-ray flux produced by DM annihilation in dSphs is proportional to J_0 and can be calculated using Eq. (23). In this case, the upper limits on the DM annihilation cross section at 95% C.L. are determined through the combined analysis using the joint likelihood $\mathcal{L}$. The results are shown in the left panel of Fig. 1. It can be seen that the resulting constraints are only marginally compatible with the region favored by the AMS-02 CR positron data.

For the s-wave Sommerfeld-enhanced DM annihilation models, the upper limits on DM annihilation cross section from Fermi-LAT gamma-ray data on dSphs have been determined in Ref. [94]. The calculation is similar to the constant cross section case, except that the J-factor J_0 should be replaced by J_s. Since the s-wave Sommerfeld enhancement factor S_0 increases monotonically with decreasing DM velocity, for s-wave Sommerfeld-enhanced DM annihilation, the corresponding upper limits are lower roughly by a factor of $S_0(v_{\rm dSphs})/S_0(v_{\rm halo}) > 1$. Thus it becomes even more difficult to reconcile the AMS-02 CR positron data and Fermi-LAT gamma-ray data in this scenario.

In p-wave Sommerfeld-enhanced DM annihilation models, the situation can be quite different. In this case, the parameter $\boldsymbol{\mu}$ corresponds to the global factor b. With the Sommerfeld-enhanced J-factor J_p calculated in the previous subsection, it is straight forward to calculate the gamma-ray flux produced by the DM annihilation in dSphs from Eq. (22).

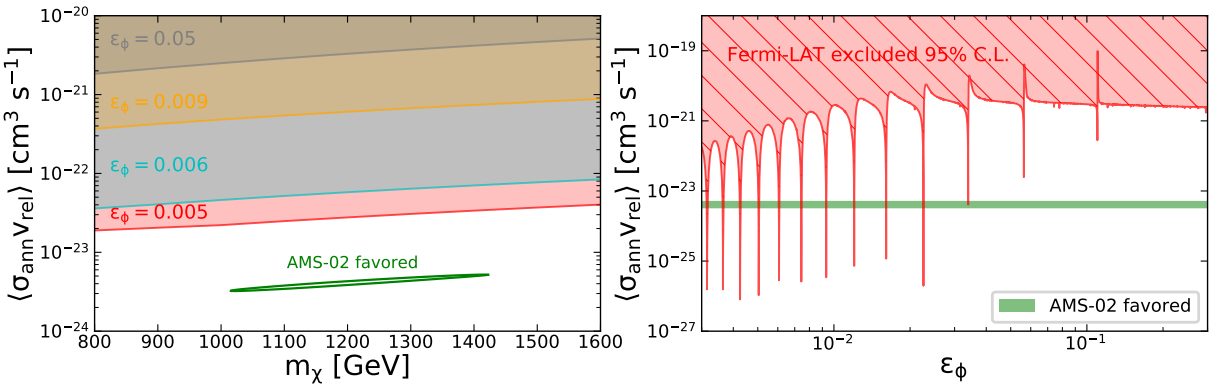


FIG. 7: Left) Upper limits on DM annihilation cross section at 95% C.L. as a function of DM particle mass m_χ derived from a combined analysis on the Fermi-LAT gamma-ray data of the 15 dSphs listed in Table. III [21] for four different values of ϵ_ϕ . The DM annihilation channel is $\chi\chi \to 2\phi \to 4\mu$. The value of the coupling strength is fixed at $\alpha = 0.2$. Right) The same upper limits as a function of ϵ_ϕ, where m_χ is fixed at 1.2 TeV. In both panels, the green regions are favored by AMS-02 CR positron data [4] at 95% C.L..

We derive the upper limits on b at 95% C.L. from the Fermi-LAT gamma-ray data as a function of m_χ for some specific values of ϵ_ϕ using the delta-log-likelihood approach. To facilitate the comparison with the AMS-02 data, we convert the obtained upper limits on the value of b to that on $\langle\sigma_{\rm ann}v_{\rm rel}\rangle$ through Eq. (16) with $v_0 = v_{\rm halo}$. In the left panel of Fig. 7, we show the upper limits for four typical values of $\epsilon_\phi = 0.005,\ 0.006,\ 0.009$, and 0.05 respectively. It can be seen that for these parameters, the limits are compatible with the region favored by the AMS-02 data. In the right panel of Fig. 7, we show the upper limits as a function of ϵ_ϕ with m_χ fixed at the best-fit value of 1.2 TeV from the AMS-02 data. In the regions very close to the resonance, the factor J_p is significantly enhanced and the constraints from the Fermi-LAT gamma-ray data become very stringent, which exclude some of the AMS-02 favored parameter region. Note that, although the successful explanation of the AMS-02 positron data and the DM thermal relic density also requires that ϵ_ϕ should be close to the resonance regions, such regions in general do not overlap with that excluded by the Fermi-LAT gamma-ray data. Thus a consistent explanation for all the observable is still possible.

VI. CONSTRAINTS FROM CMB

The recombination history of the Universe can be modified by energy injection into gas, photon-baryon plasma and background radiation from DM annihilation, which can lead to modifications in the temperature and polarization power spectra of CMB [24, 25]. Thus, the measurement on the anisotropy of CMB can be used to constrain the nature of DM

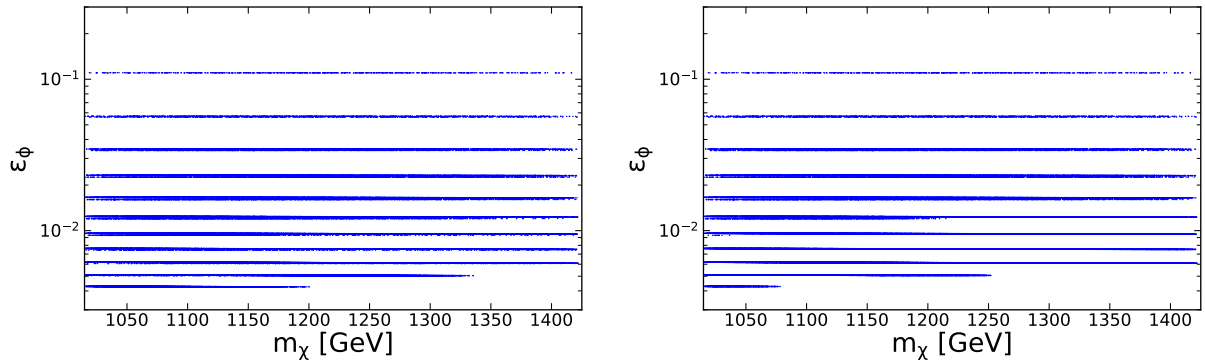


FIG. 8: Left) Parameter regions which can simultaneously account for the AMS-02 CR positron excess [4] and DM relic density [1] in the (m_χ, ϵ_ϕ) plane. The value of the coupling strength is fixed at $\alpha = 0.2$. Right) Parameter regions which can simultaneously account for the AMS-02 CR positron excess and DM relic density, and still allowed by the constraints from gamma-ray data of 15 nearby dSphs measured by Fermi-LAT [21] and CMB measured by Planck [1].

particles [28, 98, 99]. Recently, the Planck collaboration reported upper limits on the DM annihilation cross section as $f_{\rm eff}\langle\sigma_{\rm ann}v_{\rm rel}\rangle/m_\chi \leq 3.2\times10^{-28}$ cm^3 s^{-1} GeV^{-1} at 95% C.L. [1], where $f_{\rm eff}$ is an effective factor describing the fraction of energy from DM annihilation ionizing and heating the intergalactic medium. Using the value of $f_{\rm eff}\approx 0.16$ for 4μ annihilation channel [100] and assuming that $\langle\sigma_{\rm ann}v_{\rm rel}\rangle$ is velocity independent, we show in Fig. 1 the 95% C.L. upper limits on DM annihilation cross section as a function of DM particle mass from the Planck data. The constraints are apparently in strong tension with the AMS-02 favored parameter region if the cross section is velocity independent. For the s-wave Sommerfeld-enhanced DM annihilation, the constraints are expected to be even more stringent. In the case of p-wave Sommerfeld-enhanced DM annihilation, due to the extremely low DM averaged-velocity of ~ 1 m $\cdot$ s^{-1} in the epoch of recombination, the annihilation cross section is expected to be strongly suppressed by the v^2 factor, which leads to rather weak constraints from the CMB measurements.

VII. COMBINED CONSTRAINTS FROM AMS-02, RELIC DENCITY, FERIMI-LAT AND PLANCK

In order to find the proper parameter space which allows for consistent explanations for the four type of measurements: i) AMS-02 positron excess, ii) DM thermal relic density, iii) gamma rays of dSphs and iv) CMB in the p-wave Sommerfeld-enhaced DM annihilation, we perform a scan in the two-dimensional parameter space (m_χ, ϵ_ϕ) with the coupling α fixed at 0.2. The allowed parameters are those satisfying all the constraints at 95% C.L.. The allowed parameter regions are shown in Fig. 8. It can be seen that only the discrete regions with

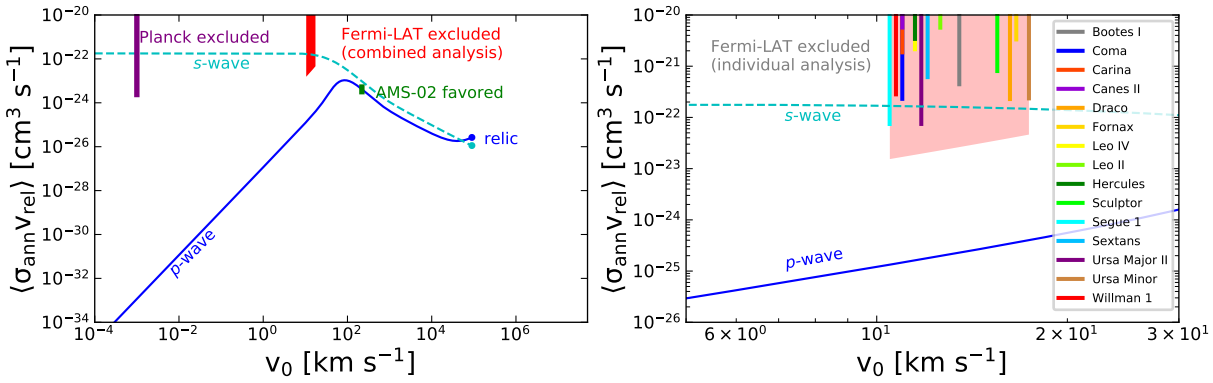


FIG. 9: Left) p-wave Sommerfeld-enhanced DM annihilation cross section as a function of the DM most probable velocity v_0 with the global factor b fixed by the DM thermal relic density (blue solid). The DM annihilation channel is $\chi\chi \to 2\phi \to 4\mu$ with $m_\chi = 1.2$ TeV, $m_\phi = 1.8$ GeV and $\alpha = 0.2$. For comparison, the case of an s-wave Sommerfeld-enhanced DM annihilation cross section calculated from Eq. (10) is also shown (cyan dashed). The green region stands for the cross section favored by AMS-02 positron data [4] with $v_0 \sim 220$ km s^{-1}. The vertical region correspond to the upper limits at 95% C.L. from a joint analysis of the 15 dSphs measured by Fermi-LAT [21] with typical $v_0 \sim 10 - 20$ km s^{-1}. The purple vertical line indicates the cross section excluded by Planck CMB observations [1] at 95% C.L. with typical $v_0 \sim 1$ m s^{-1}. Right) Constraints from individual dSphs. The vertical lines with different colors correspond to the upper limits from Fermi-LAT gamma-ray data of individual dSphs [21] at 95% C.L., where v_0 are taken to be the most probable velocity at $r = r_s/2$ for each dSph. The shaded region is excluded by the joint analysis of all the 15 dSphs.

ϵ_ϕ being close to the resonant values are allowed by the data of AMS-02 positron excess and DM relic density together. Some of regions are further excluded by the Fermi-LAT gamma-ray data as shown in the right panel of Fig. 8. We find that the CMB data from Planck impose almost no additional constraints in the p-wave Sommerfeld-enhanced DM annihilation, which is expected from the strong velocity suppression in this processes. Due to the rescaling factor of ~ 0.89 (1.48) of DM annihilation cross section favored by AMS-02 positron excess in the "MIN" ("MAX") propagation model relative to "MED" propagation model, the final parameter regions which can account for both the AMS-02 positron excess and the correct DM relic density while being in agreement with dSphs gamma-ray and CMB constraints would be away from (close to) resonances slightly, and the relevant DM mass is rescaled by a factor of ~ 0.78 (1.62).

The parameters which can successfully survive all the considered constraints correspond to the non-trivial velocity dependence of the DM annihilation cross section. For illustration purpose, we show in Fig. 9 the variation of $\langle\sigma_{\rm ann}v_{\rm rel}\rangle$ with the velocity v_0, for a typical parameters set of $m_\chi = 1.2$ TeV, $m_\phi = 1.8$ GeV and $\alpha = 0.2$. The cross section is fixed

at $\sim 3\times10^{-26}$ cm^{3}s^{-1} by the relic density at $v_0 \sim c/3 \approx 10^5$ km$\cdot$s^{-1}. When the velocity/temperature decreases, the cross section increases due to the Sommerfeld enhancement, and reaches $\sim 3\times10^{-24}$ cm^{3}s^{-1} for $v_0 \sim 220$ km$\cdot$s^{-1} which is large enough to account for the AMS-02 positron excess. The cross section continues to increase and reaches a maximal value at $v_0 \sim 90$ km$\cdot$s^{-1}, then starts to decrease towards lower v_0. At $v_0 \sim 10$ km$\cdot$s^{-1}, the cross section becomes smaller than the constraints of both the combined and individual constraint (right panel of Fig. 9) from the dSph gamma-ray data measured by Fermi-LAT. Finally at $v_0 \sim 1$ m$\cdot$s^{-1}, the cross section becomes extremely small such that the CMB cannot impose any constraints. In Fig. 9, we also show the velocity dependence for the case of s-wave Sommerfeld enhancement with the same DM and mediator mass and the cross section at high temperature fixed by the DM thermal relic density. It can be seen that although the s-wave Sommerfeld enhancement can explain the CR positron excess, it in general predicts too large cross sections at low velocities, which is in strong tensions with the dSphs gamma-ray data and the measurements of CMB.

VIII. CONSTRAINTS FROM BOUNDS-STATE FORMATION

So far we have consider the scenario where the DM particles annihilate purely through p-wave. In some DM models, there exist additional s-wave annihilation channels which are subdominant at freeze out, but gradually becomes important when the temperature is lower due to the Sommerfeld enhancement effect. A known example is the bound state formation (BSF) process. Let us consider a dark sector consisting a fermionic DM particle χ and a light scalar mediator ϕ. Due to the same long range force, DM particles at low velocity can form bound states $(\chi\bar{\chi})$ through emitting the mediator ϕ [101–104]. Although the DM annihilation into two mediators is dominated by p-wave process (assuming the interaction conserves parity), the BSF process $\chi\bar{\chi} \to (\chi\bar{\chi}) + \phi$ occurs dominantly through s-wave. The cross section for the s-wave BSF process is very small at high temperature, but can be dominant at extremely low temperature, as the p-wave DM annihilation cross section is eventually velocity suppressed. Due to the s-wave BSF process, this type of model will be stringently constrained by the data of CMB [105].

The cross section for the dominant monopole transition into the s-wave bound state in the limit $v_{\rm rel} \ll m_\phi/m_\chi$ is given by [105]

$$(\sigma_{\rm bsf} v_{\rm rel})^{\rm mono}_{n,\ell=0} = \frac{2^6\pi^3\alpha^4 e^{-4n}(L^1_{n-1}(4n))^2}{9n^3 m_\chi^2 \epsilon_\phi \sin^2(\pi/\sqrt{\epsilon_\phi})} \ , \tag{32}$$

where L is the associated Laguerre polynomial, n and ℓ are the principal and angular momentum quantum numbers of the bound state, respectively. In Eq. (32) the spin degrees of freedom for the DM particle is neglected. Including it will lead to a global factor of 1/4 from spin average of each state with quantum number n and ℓ. In the dominant ground state $(n = 1)$ formation, when the DM particle is a Dirac fermion, there exist two ground states,

spin-singlet and spin-triplet with quantum numbers $J^{PC} = 0^{-+}$ and 1^{--}, respectively. The 1^{--} state, once formed, is stable if the interaction is charge-parity conserving. The 0^{-+} state, on the other hand, can decay to mediators. If the DM particle is a Majorana fermion (i.e. $\chi = \bar{\chi}$), the ground state two-DM-particle system can only be in a spin-singlet. As a result, only 1/4 of total DM annihilation can take place via the monopole transition into the ground state. Due to the very short lifetime of the spin-singlet ground state compared with the cosmological time scale in the recombination epoch, the energy injection rate from DM annihilation through the bound state channel is assumed to be proportional to the cross section of the spin-singlet ground state formation [105].

In the models with BSF, part of the previously obtained allowed parameter space can be further excluded by the CMB data. In Fig. 8, the allowed parameter points are mainly concentrated in the regions close to resonance of p-wave Sommerfeld enhancement. We take three typical value of $\epsilon_\phi = 6.12 \times 10^{-3}, 9.49 \times 10^{-3}, 2.32 \times 10^{-2}$ from the allowed regions in Fig. 8, and show the spin-singlet ground state formation cross section as a function of m_χ with $\alpha = 0.2$ in the left panel of Fig. 10. The upper limits from the CMB data are also shown for comparison. It can be seen that the points with $\epsilon_\phi = 6.12 \times 10^{-3}$ are totally excluded by the CMB data in the whole DM mass range favored by the AMS-02 data. A portion of the DM mass range are excluded for $\epsilon_\phi = 9.49 \times 10^{-3}$, and the bound state formation cross section at $\epsilon_\phi = 2.32 \times 10^{-2}$ is still compatible with CMB constraints in the entire DM mass range. In the right panel of Fig. 10, we show the parameter regions surviving the constraints from BSF formation. It can be seen that a significant portion of the parameter space can be excluded by introducing this type of processes. However, in the generic case, the CMB data cannot exclude all the parameter space, because the resonance points for the s- and p-wave Sommerfeld enhancement are in general different, as already discussed in the previous section.

IX. CONCLUSIONS

In summary, p-wave Sommerfeld-enhanced DM annihilation can have complicated velocity dependences compared with that for the s-wave case. We have considered a scenario of Sommerfeld-enhanced p-wave DM annihilation where the DM annihilation cross section can be enhanced at certain velocities but eventually be highly suppressed when the DM velocity approaches zero. We have performed a systematic calculation of the velocity-dependent J-factors for the Sommerfeld-enhanced p-wave DM annihilation for 15 nearby dSphs, and derived constraints from the gamma-ray data of these dSphs from Fermi-LAT. We have shown that there are parameter regions where it can simultaneously account for the CR positron excess, DM relic density, gamma-ray data of dSphs from Fermi-LAT, and CMB measurements from Planck. Our results show that the CR positron excess can still be consistently explained within the WIMP scenario framework.

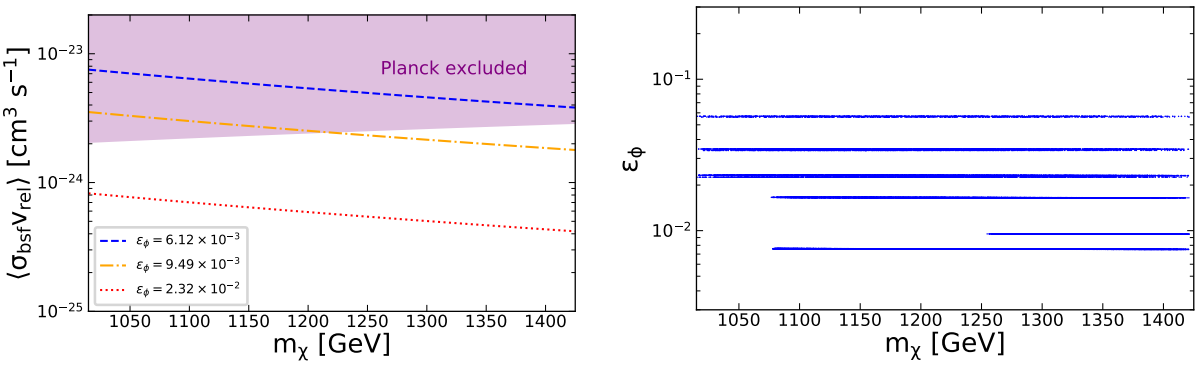


FIG. 10: Left) The spin-singlet ground state formation cross section as a function of m_χ at $\epsilon_\phi = 6.12\times10^{-3}, 9.49\times10^{-3}, 2.32\times10^{-2}$. The value of α is fixed at 0.2. The shaded region is excluded by CMB constraints from Planck [1]. Right) Parameter regions in the (m_χ, ϵ_ϕ) plane which can simultaneously account for the AMS-02 CR positron excess [4] and the correct DM relic density [1] while being in agreement with dSphs gamma-ray observations [21] and CMB constraints from the s-wave bound state formation [1].

Acknowledgments

We thank Xian-Jun Huang and Jing Chen for early involvement of this work. This work is supports in part by The National Key R&D Program of China No. 2017YFA0402204, the National Natural Science Foundation of China (NSFC) No. 11825506, No. 11821505, No. U1738209, No. 11851303, No. 11947302, the Key Research Program of the Chinese Academy of Sciences (CAS), Grant NO. XDPB15, and the CAS Project for Young Scientists in Basic Research YSBR-006.

Appendix A: Uncertainties in propagation models

In this section, we summarize the fitting results of three propagation models "MIN", "MED", and "MAX" mentioned in Sec. II. In Fig. 11, we show the regions favored by AMS-02 positron data in $(m_\chi, \langle\sigma_{\rm ann}v_{\rm rel}\rangle)$ space at 95% C.L. for the three propagation models. The posterior means, standard deviations and best-fit values of the fitting parameters and χ^2/d.o.f of each propagation model are summarized in Tab. IV.

[1] **Planck** Collaboration, N. Aghanim *et al.*, "Planck 2018 results. VI. Cosmological parameters," *Astron. Astrophys.* **641** (2020) A6, arXiv:1807.06209 [astro-ph.CO].

[2] **PAMELA** Collaboration, O. Adriani *et al.*, "Cosmic-Ray Positron Energy Spectrum Measured by PAMELA," *Phys. Rev. Lett.* **111** (2013) 081102, arXiv:1308.0133

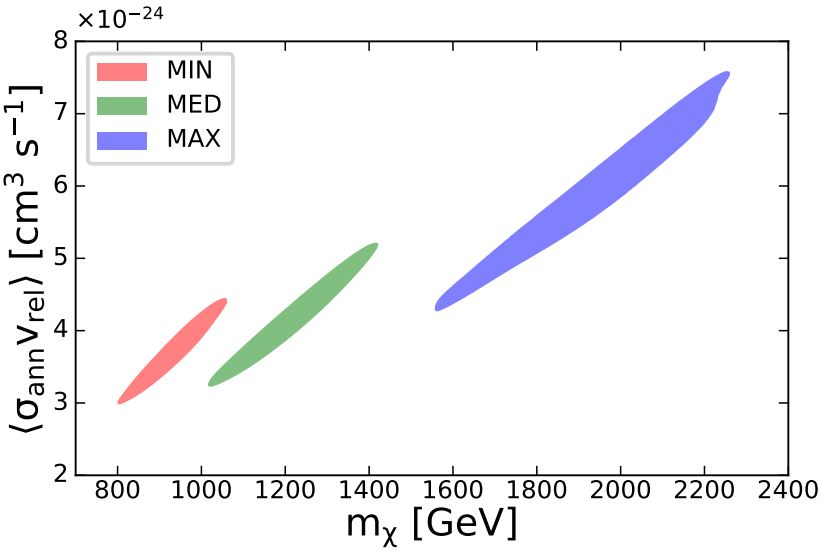


FIG. 11: Regions favored by the AMS-02 CR positron data in $(m_\chi, \langle\sigma_{\rm ann}v_{\rm rel}\rangle)$ plane for 4μ annihilaiton channel at 95% C.L. with $m_\phi = 1$ GeV. The red, green, and blue regions correspond to the "MIN", "MED", and "MAX" propagation models, respectively.

Model	$\log_{10}(m_\chi/\text{GeV})$		$\log_{10}(\langle\sigma_{\rm ann}v_{\rm rel}\rangle/\text{cm}^3\ \text{s}^{-1})$		C_{e^+}		χ^2/d.o.f
	Prior range: [1, 4]		Prior range: [-26, -21]		Prior range: [0.1, 10]		
	(Mean, σ)	Best-fit	(Mean, σ)	Best-fit	(Mean, σ)	Best-fit	
MIN	2.97 ± 0.02	2.97	-23.44 ± 0.03	-23.44	1.49 ± 0.02	1.50	56.37/32
MED	3.08 ± 0.03	3.08	-23.39 ± 0.04	-23.39	1.61 ± 0.03	1.61	31.06/32
MAX	3.30 ± 0.05	3.29	-23.22 ± 0.07	-23.22	1.69 ± 0.05	1.69	22.13/32

TABLE IV: Prior ranges, posterior means, standard deviations, and best-fit values of DM mass, annihilation cross section, and normalization factor for "MIN", "MED", and "MAX" propagation models with $m_\phi = 1$ GeV. The values of χ^2/d.o.f are also listed as an estimation of the goodness of fit.

[astro-ph.HE].

[3] **Fermi-LAT** Collaboration, M. Ackermann *et al.*, "Measurement of separate cosmic-ray electron and positron spectra with the Fermi Large Area Telescope," *Phys. Rev. Lett.* **108** (2012) 011103, arXiv:1109.0521 [astro-ph.HE].

[4] **AMS** Collaboration, M. Aguilar *et al.*, "Towards Understanding the Origin of Cosmic-Ray Positrons," *Phys. Rev. Lett.* **122** no. 4, (2019) 041102.

[5] D. Hooper, P. Blasi, and P. D. Serpico, "Pulsars as the Sources of High Energy Cosmic Ray Positrons," *JCAP* **01** (2009) 025, arXiv:0810.1527 [astro-ph].

[6] H. Yuksel, M. D. Kistler, and T. Stanev, "TeV Gamma Rays from Geminga and the Origin

of the GeV Positron Excess," *Phys. Rev. Lett.* **103** (2009) 051101, arXiv:0810.2784 [astro-ph].

[7] S. Profumo, "Dissecting cosmic-ray electron-positron data with Occam's Razor: the role of known Pulsars," *Central Eur. J. Phys.* **10** (2011) 1–31, arXiv:0812.4457 [astro-ph].

[8] D. Hooper, I. Cholis, T. Linden, and K. Fang, "HAWC Observations Strongly Favor Pulsar Interpretations of the Cosmic-Ray Positron Excess," *Phys. Rev. D* **96** no. 10, (2017) 103013, arXiv:1702.08436 [astro-ph.HE].

[9] P. Blasi, "The origin of the positron excess in cosmic rays," *Phys. Rev. Lett.* **103** (2009) 051104, arXiv:0903.2794 [astro-ph.HE].

[10] H.-B. Hu, Q. Yuan, B. Wang, C. Fan, J.-L. Zhang, and X.-J. Bi, "On the e+ e- excesses and the knee of the cosmic ray spectra - hints of cosmic rays acceleration in young supernova remnants," *Astrophys. J. Lett.* **700** (2009) L170–L173, arXiv:0901.1520 [astro-ph.HE].

[11] Y. Fujita, K. Kohri, R. Yamazaki, and K. Ioka, "Is the PAMELA anomaly caused by the supernova explosions near the Earth?," *Phys. Rev.* **D80** (2009) 063003, arXiv:0903.5298 [astro-ph.HE].

[12] L. Bergstrom, T. Bringmann, and J. Edsjo, "New Positron Spectral Features from Supersymmetric Dark Matter - a Way to Explain the PAMELA Data?," *Phys. Rev.* **D78** (2008) 103520, arXiv:0808.3725 [astro-ph].

[13] M. Cirelli, M. Kadastik, M. Raidal, and A. Strumia, "Model-independent implications of the e+-, anti-proton cosmic ray spectra on properties of Dark Matter," *Nucl. Phys.* **B813** (2009) 1–21, arXiv:0809.2409 [hep-ph]. [Addendum: Nucl. Phys.B873,530(2013)].

[14] L. Bergstrom, J. Edsjo, and G. Zaharijas, "Dark matter interpretation of recent electron and positron data," *Phys. Rev. Lett.* **103** (2009) 031103, arXiv:0905.0333 [astro-ph.HE].

[15] S.-J. Lin, Q. Yuan, and X.-J. Bi, "Quantitative study of the AMS-02 electron/positron spectra: Implications for pulsars and dark matter properties," *Phys. Rev.* **D91** no. 6, (2015) 063508, arXiv:1409.6248 [astro-ph.HE].

[16] H.-B. Jin, Y.-L. Wu, and Y.-F. Zhou, "Implications of the first AMS-02 measurement for dark matter annihilation and decay," *JCAP* **1311** (2013) 026, arXiv:1304.1997 [hep-ph].

[17] H.-B. Jin, Y.-L. Wu, and Y.-F. Zhou, "Cosmic ray propagation and dark matter in light of the latest AMS-02 data," *JCAP* **09** (2015) 049, arXiv:1410.0171 [hep-ph].

[18] I. Cholis, L. Goodenough, D. Hooper, M. Simet, and N. Weiner, "High Energy Positrons From Annihilating Dark Matter," *Phys. Rev. D* **80** (2009) 123511, arXiv:0809.1683 [hep-ph].

[19] M. Cirelli, P. Panci, and P. D. Serpico, "Diffuse gamma ray constraints on annihilating or decaying Dark Matter after Fermi," *Nucl. Phys. B* **840** (2010) 284–303, arXiv:0912.0663 [astro-ph.CO].

[20] **AMS** Collaboration, M. Aguilar *et al.*, "Antiproton Flux, Antiproton-to-Proton Flux

Ratio, and Properties of Elementary Particle Fluxes in Primary Cosmic Rays Measured with the Alpha Magnetic Spectrometer on the International Space Station," *Phys. Rev. Lett.* **117** no. 9, (2016) 091103.

[21] **Fermi-LAT** Collaboration, M. Ackermann *et al.*, "Searching for Dark Matter Annihilation from Milky?Way Dwarf Spheroidal Galaxies with Six Years of Fermi Large Area Telescope Data," *Phys. Rev. Lett.* **115** no. 23, (2015) 231301, arXiv:1503.02641 [astro-ph.HE].

[22] J. Diemand, M. Kuhlen, P. Madau, M. Zemp, B. Moore, D. Potter, and J. Stadel, "Clumps and streams in the local dark matter distribution," *Nature* **454** (2008) 735–738, arXiv:0805.1244 [astro-ph].

[23] V. Springel, S. D. M. White, C. S. Frenk, J. F. Navarro, A. Jenkins, M. Vogelsberger, J. Wang, A. Ludlow, and A. Helmi, "A blueprint for detecting supersymmetric dark matter in the Galactic halo," arXiv:0809.0894 [astro-ph].

[24] X.-L. Chen and M. Kamionkowski, "Particle decays during the cosmic dark ages," *Phys. Rev.* **D70** (2004) 043502, arXiv:astro-ph/0310473 [astro-ph].

[25] N. Padmanabhan and D. P. Finkbeiner, "Detecting dark matter annihilation with CMB polarization: Signatures and experimental prospects," *Phys. Rev.* **D72** (2005) 023508, arXiv:astro-ph/0503486 [astro-ph].

[26] T. R. Slatyer, "Indirect Dark Matter Signatures in the Cosmic Dark Ages II. Ionization, Heating and Photon Production from Arbitrary Energy Injections," *Phys. Rev.* **D93** no. 2, (2016) 023521, arXiv:1506.03812 [astro-ph.CO].

[27] T. R. Slatyer, "Indirect dark matter signatures in the cosmic dark ages. I. Generalizing the bound on s-wave dark matter annihilation from Planck results," *Phys. Rev. D* **93** no. 2, (2016) 023527, arXiv:1506.03811 [hep-ph].

[28] S. Galli, F. Iocco, G. Bertone, and A. Melchiorri, "CMB constraints on Dark Matter models with large annihilation cross-section," *Phys. Rev.* **D80** (2009) 023505, arXiv:0905.0003 [astro-ph.CO].

[29] A. Sommerfeld, "Über die beugung und bremsung der elektronen," *Annalen der Physik* **403** no. 3, (1931) 257–330.

[30] J. Hisano, S. Matsumoto, and M. M. Nojiri, "Explosive dark matter annihilation," *Phys. Rev. Lett.* **92** (2004) 031303, arXiv:hep-ph/0307216 [hep-ph].

[31] J. Hisano, S. Matsumoto, and M. M. Nojiri, "Unitarity and higher order corrections in neutralino dark matter annihilation into two photons," *Phys. Rev. D* **67** (2003) 075014, arXiv:hep-ph/0212022.

[32] M. Cirelli, A. Strumia, and M. Tamburini, "Cosmology and Astrophysics of Minimal Dark Matter," *Nucl. Phys.* **B787** (2007) 152–175, arXiv:0706.4071 [hep-ph].

[33] N. Arkani-Hamed, D. P. Finkbeiner, T. R. Slatyer, and N. Weiner, "A Theory of Dark Matter," *Phys. Rev.* **D79** (2009) 015014, arXiv:0810.0713 [hep-ph].

[34] M. Pospelov and A. Ritz, "Astrophysical Signatures of Secluded Dark Matter," *Phys. Lett.*

B **671** (2009) 391–397, arXiv:0810.1502 [hep-ph].

[35] J. D. March-Russell and S. M. West, "WIMPonium and Boost Factors for Indirect Dark Matter Detection," *Phys. Lett. B* **676** (2009) 133–139, arXiv:0812.0559 [astro-ph].

[36] R. Iengo, "Sommerfeld enhancement: General results from field theory diagrams," *JHEP* **05** (2009) 024, arXiv:0902.0688 [hep-ph].

[37] S. Cassel, "Sommerfeld factor for arbitrary partial wave processes," *J. Phys.* **G37** (2010) 105009, arXiv:0903.5307 [hep-ph].

[38] J. Hisano, S. Matsumoto, M. Nagai, O. Saito, and M. Senami, "Non-perturbative effect on thermal relic abundance of dark matter," *Phys. Lett.* **B646** (2007) 34–38, arXiv:hep-ph/0610249 [hep-ph].

[39] M. Lattanzi and J. I. Silk, "Can the WIMP annihilation boost factor be boosted by the Sommerfeld enhancement?," *Phys. Rev.* **D79** (2009) 083523, arXiv:0812.0360 [astro-ph].

[40] Z.-P. Liu, Y.-L. Wu, and Y.-F. Zhou, "Sommerfeld enhancements with vector, scalar and pseudoscalar force-carriers," *Phys. Rev.* **D88** (2013) 096008, arXiv:1305.5438 [hep-ph].

[41] J. L. Feng, M. Kaplinghat, and H.-B. Yu, "Sommerfeld Enhancements for Thermal Relic Dark Matter," *Phys. Rev.* **D82** (2010) 083525, arXiv:1005.4678 [hep-ph].

[42] D. P. Finkbeiner, L. Goodenough, T. R. Slatyer, M. Vogelsberger, and N. Weiner, "Consistent Scenarios for Cosmic-Ray Excesses from Sommerfeld-Enhanced Dark Matter Annihilation," *JCAP* **05** (2011) 002, arXiv:1011.3082 [hep-ph].

[43] J. Zavala, M. Vogelsberger, and S. D. M. White, "Relic density and CMB constraints on dark matter annihilation with Sommerfeld enhancement," *Phys. Rev.* **D81** (2010) 083502, arXiv:0910.5221 [astro-ph.CO].

[44] S. Hannestad and T. Tram, "Sommerfeld Enhancement of DM Annihilation: Resonance Structure, Freeze-Out and CMB Spectral Bound," *JCAP* **01** (2011) 016, arXiv:1008.1511 [astro-ph.CO].

[45] J. Hisano, M. Kawasaki, K. Kohri, T. Moroi, K. Nakayama, and T. Sekiguchi, "Cosmological constraints on dark matter models with velocity-dependent annihilation cross section," *Phys. Rev. D* **83** (2011) 123511, arXiv:1102.4658 [hep-ph].

[46] M. Kamionkowski and S. Profumo, "Early Annihilation and Diffuse Backgrounds in Models of Weakly Interacting Massive Particles in Which the Cross Section for Pair Annihilation Is Enhanced by 1/v," *Phys. Rev. Lett.* **101** (2008) 261301, arXiv:0810.3233 [astro-ph].

[47] J. Bovy, "Substructure Boosts to Dark Matter Annihilation from Sommerfeld Enhancement," *Phys. Rev. D* **79** (2009) 083539, arXiv:0903.0413 [astro-ph.HE].

[48] M. R. Buckley and P. J. Fox, "Dark Matter Self-Interactions and Light Force Carriers," *Phys. Rev.* **D81** (2010) 083522, arXiv:0911.3898 [hep-ph].

[49] J. L. Feng, M. Kaplinghat, and H.-B. Yu, "Halo Shape and Relic Density Exclusions of Sommerfeld-Enhanced Dark Matter Explanations of Cosmic Ray Excesses," *Phys. Rev.*

Lett. **104** (2010) 151301, arXiv:0911.0422 [hep-ph].

[50] I. Cholis and L. Goodenough, "Consequences of a Dark Disk for the Fermi and PAMELA Signals in Theories with a Sommerfeld Enhancement," *JCAP* **09** (2010) 010, arXiv:1006.2089 [astro-ph.HE].

[51] B. Robertson and A. Zentner, "Dark Matter Annihilation Rates with Velocity-Dependent Annihilation Cross Sections," *Phys. Rev. D* **79** (2009) 083525, arXiv:0902.0362 [astro-ph.CO].

[52] M. Cirelli and J. M. Cline, "Can multistate dark matter annihilation explain the high-energy cosmic ray lepton anomalies?," *Phys. Rev.* **D82** (2010) 023503, arXiv:1005.1779 [hep-ph].

[53] K. N. Abazajian and J. P. Harding, "Constraints on WIMP and Sommerfeld-Enhanced Dark Matter Annihilation from HESS Observations of the Galactic Center," *JCAP* **01** (2012) 041, arXiv:1110.6151 [hep-ph].

[54] **H.E.S.S.** Collaboration, H. Abdallah *et al.*, "Search for dark matter annihilations towards the inner Galactic halo from 10 years of observations with H.E.S.S," *Phys. Rev. Lett.* **117** no. 11, (2016) 111301, arXiv:1607.08142 [astro-ph.HE].

[55] **Fermi-LAT** Collaboration, M. Ackermann *et al.*, "Limits on Dark Matter Annihilation Signals from the Fermi LAT 4-year Measurement of the Isotropic Gamma-Ray Background," *JCAP* **09** (2015) 008, arXiv:1501.05464 [astro-ph.CO].

[56] **H.E.S.S.** Collaboration, A. Abramowski *et al.*, "Constraints on an Annihilation Signal from a Core of Constant Dark Matter Density around the Milky Way Center with H.E.S.S.," *Phys. Rev. Lett.* **114** no. 8, (2015) 081301, arXiv:1502.03244 [astro-ph.HE].

[57] M. Boylan-Kolchin, V. Springel, S. D. M. White, A. Jenkins, and G. Lemson, "Resolving Cosmic Structure Formation with the Millennium-II Simulation," *Mon. Not. Roy. Astron. Soc.* **398** (2009) 1150, arXiv:0903.3041 [astro-ph.CO].

[58] **Fermi-LAT** Collaboration, A. A. Abdo *et al.*, "Constraints on Cosmological Dark Matter Annihilation from the Fermi-LAT Isotropic Diffuse Gamma-Ray Measurement," *JCAP* **04** (2010) 014, arXiv:1002.4415 [astro-ph.CO].

[59] J. Wang, S. Bose, C. S. Frenk, L. Gao, A. Jenkins, V. Springel, and S. D. M. White, "Universal structure of dark matter haloes over a mass range of 20 orders of magnitude," *Nature* **585** no. 7823, (2020) 39–42, arXiv:1911.09720 [astro-ph.CO].

[60] P.-f. Yin, Q. Yuan, J. Liu, J. Zhang, X.-j. Bi, and S.-h. Zhu, "PAMELA data and leptonically decaying dark matter," *Phys. Rev.* **D79** (2009) 023512, arXiv:0811.0176 [hep-ph].

[61] V. S. Berezinsky, S. V. Bulanov, V. A. Dogiel, and V. S. Ptuskin, *Astrophysics of cosmic rays*. 1990.

[62] A. W. Strong, I. V. Moskalenko, and V. S. Ptuskin, "Cosmic-ray propagation and interactions in the Galaxy," *Ann. Rev. Nucl. Part. Sci.* **57** (2007) 285–327,

arXiv:astro-ph/0701517 [astro-ph].

[63] G. Case and D. Bhattacharya, *Revisiting the galactic supernova remnant distribution.*, vol. 120. Dec., 1996.

[64] A. W. Strong and I. V. Moskalenko, "Propagation of cosmic-ray nucleons in the galaxy," *Astrophys. J.* **509** (1998) 212–228, arXiv:astro-ph/9807150 [astro-ph].

[65] I. V. Moskalenko, A. W. Strong, J. F. Ormes, and M. S. Potgieter, "Secondary anti-protons and propagation of cosmic rays in the galaxy and heliosphere," *Astrophys. J.* **565** (2002) 280–296, arXiv:astro-ph/0106567 [astro-ph].

[66] A. W. Strong and I. V. Moskalenko, "Models for galactic cosmic ray propagation," *Adv. Space Res.* **27** (2001) 717–726, arXiv:astro-ph/0101068 [astro-ph].

[67] I. V. Moskalenko, A. W. Strong, S. G. Mashnik, and J. F. Ormes, "Challenging cosmic ray propagation with antiprotons. Evidence for a fresh nuclei component?," *Astrophys. J.* **586** (2003) 1050–1066, arXiv:astro-ph/0210480 [astro-ph].

[68] V. S. Ptuskin, I. V. Moskalenko, F. C. Jones, A. W. Strong, and V. N. Zirakashvili, "Dissipation of magnetohydrodynamic waves on energetic particles: impact on interstellar turbulence and cosmic ray transport," *Astrophys. J.* **642** (2006) 902–916, arXiv:astro-ph/0510335 [astro-ph].

[69] J. Einasto, "Dark Matter," in *Astronomy and Astrophysics 2010, [Eds. Oddbjorn Engvold, Rolf Stabell, Bozena Czerny, John Lattanzio], in Encyclopedia of Life Support Systems (EOLSS), Developed under the Auspices of the UNESCO, Eolss Publishers, Oxford ,UK.* 2009. arXiv:0901.0632 [astro-ph.CO].

[70] P. Salucci, F. Nesti, G. Gentile, and C. F. Martins, "The dark matter density at the Sun's location," *Astron. Astrophys.* **523** (2010) A83, arXiv:1003.3101 [astro-ph.GA].

[71] B. Batell, N. Lange, D. McKeen, M. Pospelov, and A. Ritz, "Muon anomalous magnetic moment through the leptonic Higgs portal," *Phys. Rev. D* **95** no. 7, (2017) 075003, arXiv:1606.04943 [hep-ph].

[72] G. D'Ambrosio, G. F. Giudice, G. Isidori, and A. Strumia, "Minimal flavor violation: An Effective field theory approach," *Nucl. Phys. B* **645** (2002) 155–187, arXiv:hep-ph/0207036.

[73] B. Batell, A. Freitas, A. Ismail, and D. Mckeen, "Flavor-specific scalar mediators," *Phys. Rev. D* **98** no. 5, (2018) 055026, arXiv:1712.10022 [hep-ph].

[74] L. Marsicano, M. Battaglieri, A. Celentano, R. De Vita, and Y.-M. Zhong, "Probing Leptophilic Dark Sectors at Electron Beam-Dump Facilities," *Phys. Rev. D* **98** no. 11, (2018) 115022, arXiv:1812.03829 [hep-ex].

[75] T. Sjöstrand, S. Ask, J. R. Christiansen, R. Corke, N. Desai, P. Ilten, S. Mrenna, S. Prestel, C. O. Rasmussen, and P. Z. Skands, "An Introduction to PYTHIA 8.2," *Comput. Phys. Commun.* **191** (2015) 159–177, arXiv:1410.3012 [hep-ph].

[76] F. Feroz and M. Hobson, "Multimodal nested sampling: an efficient and robust alternative

to MCMC methods for astronomical data analysis," *Mon. Not. Roy. Astron. Soc.* **384** (2008) 449, arXiv:0704.3704 [astro-ph].

[77] F. Feroz, M. Hobson, and M. Bridges, "MultiNest: an efficient and robust Bayesian inference tool for cosmology and particle physics," *Mon. Not. Roy. Astron. Soc.* **398** (2009) 1601–1614, arXiv:0809.3437 [astro-ph].

[78] F. Feroz, M. Hobson, E. Cameron, and A. Pettitt, "Importance Nested Sampling and the MultiNest Algorithm," arXiv:1306.2144 [astro-ph.IM].

[79] S. Tulin, H.-B. Yu, and K. M. Zurek, "Beyond Collisionless Dark Matter: Particle Physics Dynamics for Dark Matter Halo Structure," *Phys. Rev.* **D87** no. 11, (2013) 115007, arXiv:1302.3898 [hep-ph].

[80] G. Bertone, D. Hooper, and J. Silk, "Particle dark matter: Evidence, candidates and constraints," *Phys. Rept.* **405** (2005) 279–390, arXiv:hep-ph/0404175 [hep-ph].

[81] E. W. Kolb and M. S. Turner, eds., *THE EARLY UNIVERSE. REPRINTS.* 1988.

[82] G. Steigman, B. Dasgupta, and J. F. Beacom, "Precise Relic WIMP Abundance and its Impact on Searches for Dark Matter Annihilation," *Phys. Rev.* **D86** (2012) 023506, arXiv:1204.3622 [hep-ph].

[83] J. Chen and Y.-F. Zhou, "The 130 GeV gamma-ray line and Sommerfeld enhancements," *JCAP* **1304** (2013) 017, arXiv:1301.5778 [hep-ph].

[84] G. Jungman, M. Kamionkowski, and K. Griest, "Supersymmetric dark matter," *Phys. Rept.* **267** (1996) 195–373, arXiv:hep-ph/9506380 [hep-ph].

[85] J. Grcevich and M. E. Putman, "HI in Local Group Dwarf Galaxies and Stripping by the Galactic Halo," *Astrophys. J.* **696** (2009) 385–395, arXiv:0901.4975 [astro-ph.GA]. [Erratum: Astrophys. J.721,922(2010)].

[86] J. Binney and S. Tremaine, *Galactic Dynamics: Second Edition.* 2008.

[87] J. F. Navarro, C. S. Frenk, and S. D. M. White, "A Universal density profile from hierarchical clustering," *Astrophys. J.* **490** (1997) 493–508, arXiv:astro-ph/9611107 [astro-ph].

[88] G. D. Martinez, "A robust determination of Milky Way satellite properties using hierarchical mass modelling," *Mon. Not. Roy. Astron. Soc.* **451** no. 3, (2015) 2524–2535, arXiv:1309.2641 [astro-ph.GA].

[89] M. Kuhlen, M. Vogelsberger, and R. Angulo, "Numerical Simulations of the Dark Universe: State of the Art and the Next Decade," *Phys. Dark Univ.* **1** (2012) 50–93, arXiv:1209.5745 [astro-ph.CO].

[90] J. Diemand and B. Moore, "The structure and evolution of cold dark matter halos," *Adv. Sci. Lett.* **4** (2011) 297–310, arXiv:0906.4340 [astro-ph.CO].

[91] W. J. G. de Blok, "The Core-Cusp Problem," *Adv. Astron.* **2010** (2010) 789293, arXiv:0910.3538 [astro-ph.CO].

[92] **Fermi-LAT** Collaboration, M. Ackermann *et al.*, "Dark matter constraints from

observations of 25 Milky Way satellite galaxies with the Fermi Large Area Telescope," *Phys. Rev.* **D89** (2014) 042001, arXiv:1310.0828 [astro-ph.HE].

[93] K. K. Boddy, J. Kumar, L. E. Strigari, and M.-Y. Wang, "Sommerfeld-Enhanced J-Factors For Dwarf Spheroidal Galaxies," *Phys. Rev.* **D95** no. 12, (2017) 123008, arXiv:1702.00408 [astro-ph.CO].

[94] B.-Q. Lu, Y.-L. Wu, W.-H. Zhang, and Y.-F. Zhou, "Constraints on the Sommerfeld-enhanced dark matter annihilation from the gamma rays of subhalos and dwarf galaxies," *JCAP* **1804** no. 04, (2018) 035, arXiv:1711.00749 [astro-ph.HE].

[95] G. D. Martinez, J. S. Bullock, M. Kaplinghat, L. E. Strigari, and R. Trotta, "Indirect Dark Matter Detection from Dwarf Satellites: Joint Expectations from Astrophysics and Supersymmetry," *JCAP* **06** (2009) 014, arXiv:0902.4715 [astro-ph.HE].

[96] L. E. Strigari, "Galactic Searches for Dark Matter," *Phys. Rept.* **531** (2013) 1–88, arXiv:1211.7090 [astro-ph.CO].

[97] http://www-glast.stanford.edu/pub_data/1048/.

[98] T. R. Slatyer, N. Padmanabhan, and D. P. Finkbeiner, "CMB Constraints on WIMP Annihilation: Energy Absorption During the Recombination Epoch," *Phys. Rev.* **D80** (2009) 043526, arXiv:0906.1197 [astro-ph.CO].

[99] D. P. Finkbeiner, S. Galli, T. Lin, and T. R. Slatyer, "Searching for Dark Matter in the CMB: A Compact Parameterization of Energy Injection from New Physics," *Phys. Rev.* **D85** (2012) 043522, arXiv:1109.6322 [astro-ph.CO].

[100] M. S. Madhavacheril, N. Sehgal, and T. R. Slatyer, "Current Dark Matter Annihilation Constraints from CMB and Low-Redshift Data," *Phys. Rev.* **D89** (2014) 103508, arXiv:1310.3815 [astro-ph.CO].

[101] K. Petraki, M. Postma, and M. Wiechers, "Dark-matter bound states from Feynman diagrams," *JHEP* **06** (2015) 128, arXiv:1505.00109 [hep-ph].

[102] H. An, M. B. Wise, and Y. Zhang, "Effects of Bound States on Dark Matter Annihilation," *Phys. Rev. D* **93** no. 11, (2016) 115020, arXiv:1604.01776 [hep-ph].

[103] M. Cirelli, P. Panci, K. Petraki, F. Sala, and M. Taoso, "Dark Matter's secret liaisons: phenomenology of a dark U(1) sector with bound states," *JCAP* **1705** no. 05, (2017) 036, arXiv:1612.07295 [hep-ph].

[104] K. Petraki, M. Postma, and J. de Vries, "Radiative bound-state-formation cross-sections for dark matter interacting via a Yukawa potential," *JHEP* **04** (2017) 077, arXiv:1611.01394 [hep-ph].

[105] H. An, M. B. Wise, and Y. Zhang, "Strong CMB Constraint On P-Wave Annihilating Dark Matter," *Phys. Lett. B* **773** (2017) 121–124, arXiv:1606.02305 [hep-ph].

[106] **Fermi-LAT** Collaboration, A. A. Abdo *et al.*, "Constraints on Cosmological Dark Matter Annihilation from the Fermi-LAT Isotropic Diffuse Gamma-Ray Measurement," *JCAP* **1004** (2010) 014, arXiv:1002.4415 [astro-ph.CO].